

Extracting a less model dependent cosmic ray composition from X_{\max} distributions

Simon Blaess, Jose A. Bellido, and Bruce R. Dawson
Department of Physics, University of Adelaide, Adelaide, Australia

At higher energies the uncertainty in the estimated cosmic ray mass composition, extracted from the observed distributions of the depth of shower maximum X_{\max} , is dominated by uncertainties in the hadronic interaction models. Thus, the estimated composition depends strongly on the particular model used for its interpretation. To reduce this model dependency in the interpretation of the mass composition, we have developed a novel approach which allows the adjustment of the normalisation levels of the proton $\langle X_{\max} \rangle$ and $\sigma(X_{\max})$ guided by real observations of X_{\max} distributions. In this paper we describe the details of this approach and present a study of its performance and its limitations. Using this approach we extracted cosmic ray mass composition information from the published Pierre Auger X_{\max} distributions. We have obtained a consistent mass composition interpretation for Epos-LHC, QGSJetII-04 and Sibyll2.3. Our fits suggest a composition consisting of predominantly iron. Below $10^{18.8}$ eV, the small proportions of proton, helium and nitrogen vary. Above $10^{18.8}$ eV, there is little proton or helium, and with increasing energy the nitrogen component gradually gives way to the growing iron component, which dominates at the highest energies. The fits suggest that the normalisation level for proton $\langle X_{\max} \rangle$ is much deeper than the initial predictions of the hadronic interaction models. The fitted normalisation level for proton $\sigma(X_{\max})$ is also greater than the model predictions. When fixing the expected normalisation of $\sigma(X_{\max})$ to that suggested by the QGSJetII-04 model, a slightly larger fraction of protons is obtained. These results remain sensitive to the other model parameters that we keep fixed, such as the elongation rate and the $\langle X_{\max} \rangle$ separation between p and Fe.

I. INTRODUCTION

A common parameter used to extract mass composition information is X_{\max} , the atmospheric depth in g/cm^2 from the top of the atmosphere where the longitudinal development of an air shower reaches the maximum number of particles or the maximum of the energy deposited in the atmosphere. Different cosmic ray primaries propagate through the atmosphere differently, resulting in different observed distributions of X_{\max} [1]. Due to statistical variability in the interaction between cosmic rays of a specific primary mass and the atmosphere, a cosmic ray's primary mass cannot be determined on an event by event basis by examining X_{\max} . Instead we study the X_{\max} distribution of cosmic rays of similar energy to infer the mass composition distribution of the events. Differences in the mode, width and tail of the X_{\max} distribution provide information on the mass composition distribution of the events and on the hadronic interaction properties [2, 3].

Fig. 1 shows the X_{\max} distribution resulting from the CONEX v4r37 simulation of 750 proton events according to the Epos-LHC model, and separately 750 proton events according to the QGSJetII-04 model, of energy 10^{18} eV. The figure illustrates the differences in the X_{\max} distribution predicted by different hadronic interaction models. Most noticeable is the difference in the modes of the distributions, but there are also marginal differences in the width and tails of the distributions. These differences between the hadronic interaction models change with energy to some degree. Although the dissimilarity between these predicted distributions may appear minor, applying a parameterisation based on these different predictions to data can have a considerable impact on the

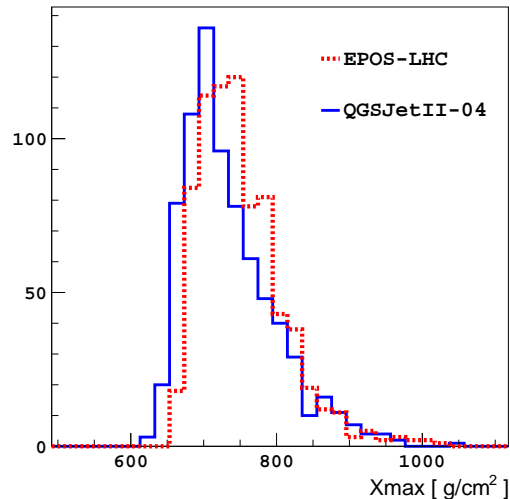


FIG. 1: An X_{\max} distribution of 750 Epos-LHC simulated proton events (red), and separately 750 QGSJetII-04 simulated protons events (blue), of energy 10^{18} eV.

mass composition inferred. Consequently, typical mass composition studies of X_{\max} are strongly dependent on the hadronic interaction model assumed.

The algorithm CONEX v4r37 [4, 5], along with the hadronic interaction packages Epos-LHC [6], QGSJetII-04 [7] and Sibyll2.3 [8], were used to simulate air showers to obtain X_{\max} distributions according to each of these models. We have developed a parameterisation for describing these expected X_{\max} distributions for cosmic rays of some energy and mass. Our parameterisation of the

X_{\max} distributions can then be used to fit observed X_{\max} distributions, to extract primary mass information (composition fractions) from each energy bin. By including some of the coefficients of our X_{\max} parameterisation in the fit, mass composition results are obtained which are somewhat independent of the hadronic interaction model assumed.

Assuming the Epos-LHC, QGSJetII-04 or Sibyll2.3 hadronic models, the Auger X_{\max} distributions can be well reproduced assuming a composition of at least four components consisting of proton, Helium, Nitrogen and Iron [9–11]. Therefore, in this work we have used mock data sets to evaluate the performance of our method for retrieving the true relative amounts of p, He, N, Fe (composition fractions). The results of applying this method to interpret the published Auger X_{\max} distributions in [9] in terms of the mass composition of cosmic rays are presented.

II. PARAMETERISATION OF X_{\max} DISTRIBUTIONS

An X_{\max} distribution of some primary energy and mass can be modelled as the convolution of a Gaussian with an exponential [12]. Three shape parameters (t_0, σ, λ) define the X_{\max} distribution:

$$\frac{dN}{dX_{\max}}(t) = \frac{1}{2\lambda} \exp\left(\frac{t_0 - t}{\lambda} + \frac{\sigma^2}{2\lambda^2}\right) \text{Erfc}\left(\frac{t_0 - t + \frac{\sigma^2}{\lambda}}{\sigma\sqrt{2}}\right) \quad (1)$$

where t_0 defines the mode of the Gaussian component, σ defines the width of the Gaussian component and λ defines the exponential tail of the X_{\max} distribution, and t is the X_{\max} bin. The mode and spread of the distribution defined in Equation (1) is sensitive to t_0 and σ respectively.

We fit Equation (1) to the X_{\max} distributions from CONEX v4r37 simulations of cosmic rays of a particular primary energy, mass (either proton, Helium, Nitrogen or Iron primaries) and hadronic interaction model, obtaining the values of t_0 , σ and λ for that distribution (see Appendix A). The fit results as a function of energy are displayed in Figs. 2, 3 and 4. The solid lines are fits to the shape parameters (t_0 , σ and λ) as a function of energy. The functions fitted are defined as follows:

$$\begin{aligned} t_0(E) &= t_{0,\text{norm}} + B \cdot \log_{10}\left(\frac{\log_{10} E}{\log_{10} E_0}\right), \\ \sigma(E) &= \sigma_{\text{norm}} + C \cdot \log_{10}\left(\frac{E}{E_0}\right), \\ \lambda(E) &= \lambda_{\text{norm}} - K + K \cdot \left(\frac{\log_{10} E}{\log_{10} E_0}\right)^{\frac{L}{\ln 10}}, \end{aligned} \quad (2)$$

where E is the energy in eV and $E_0 = 10^{18.24}$ eV, the energy at which we choose to normalise the equations. This energy corresponds to the energy at which Auger

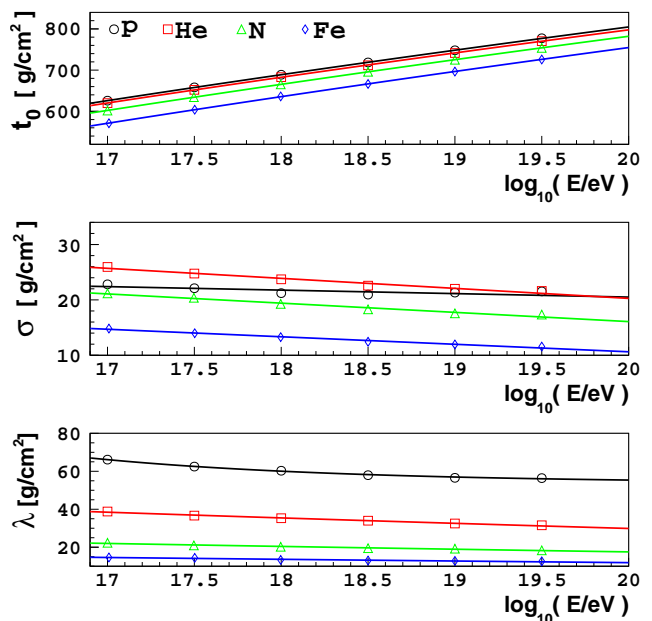


FIG. 2: Fits to the shape parameter as a function of energy according to the Epos-LHC model.

has measured λ for a proton dominated composition [3]. This means that λ_{norm} for proton can be directly compared with Λ_η , the exponential tail measured by Auger, which is shown in Equation (3). We even considered adopting Λ_η as the value for λ_{norm} , but this could potentially break self consistency in the models.

$$\Lambda_\eta = [55.8 \pm 2.3(\text{stat}) \pm 1.6(\text{sys})] \text{ g/cm}^2 \quad (3)$$

The coefficients in Equation (2) are specified in Appendix C for each mass component and hadronic model.

The functions of Equation (2) consist of two parts, the first part defining the value of a shape parameter at the normalisation energy, and the second part defining the change in the shape parameter as a function of energy. For example, for protons $t_{0,\text{norm}}$ would be the value of t_0 for protons at $10^{18.24}$ eV, and similarly σ_{norm} would be the value of σ at $10^{18.24}$ eV.

A. Accounting for the detector resolution and acceptance

The expected X_{\max} distributions are affected by the detector resolution and the detector acceptance. The Pierre Auger X_{\max} publication [9] provides parameterisations for the average detector X_{\max} resolution as a function of energy ($Res(E)$) and the detector acceptance as a function of X_{\max} for each energy bin, $Acc(E, t)$, where t is the X_{\max} bin as in Equation (1).

The detector X_{\max} resolution is accounted for by adding it in quadrature with the corresponding $\sigma(E)$, to provide the total expected value of $\sigma(E)_{\text{tot}}$ for some

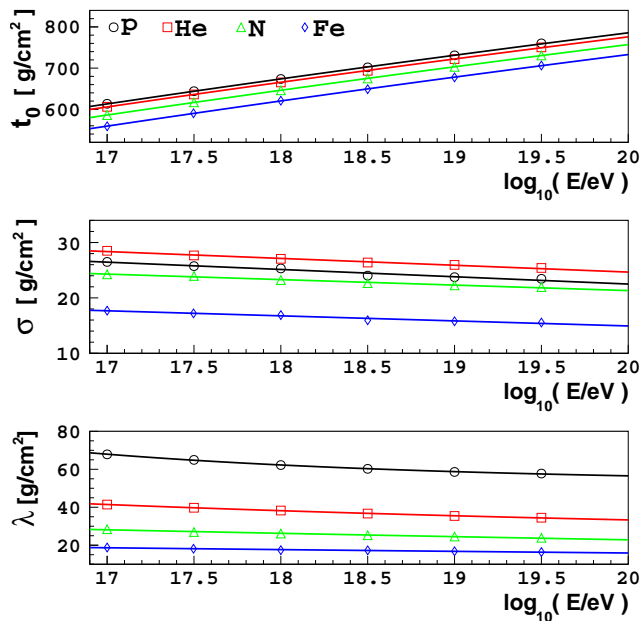


FIG. 3: Fits to the shape parameter as a function of energy according to the QGSJetII-04 model.

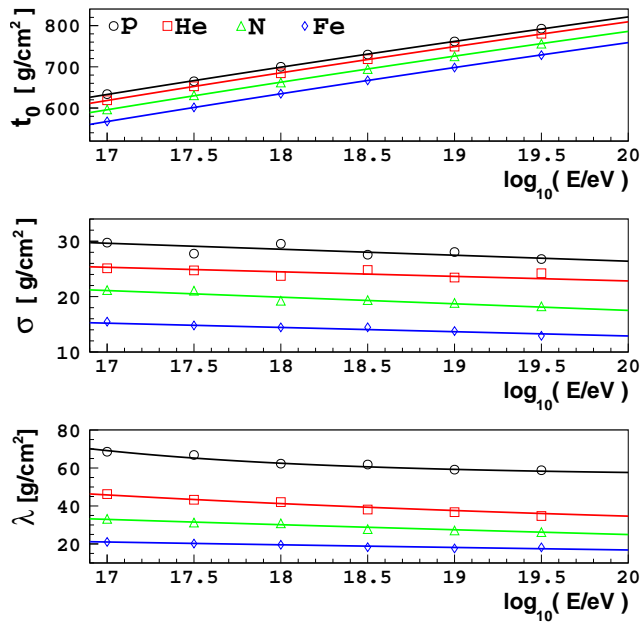


FIG. 4: Fits to the shape parameter as a function of energy according to the Sibyll2.3 model.

primary:

$$\sigma(E)_{tot} = \sqrt{\sigma(E)^2 + Res(E)^2} \quad (4)$$

We can combine Equations (1), (2), (4) and the detector acceptance $Acc(E, t)$ to obtain the expected X_{max} distribution for cosmic rays of a mixture of primary masses in a particular energy bin according to a hadronic interaction model:

$$\left. \frac{dN}{dX_{max}}(E, t) \right|_{total} = N(E) Acc(E, t) \sum_{i=p, He, N, Fe} f_i(E) \left. \frac{dN}{dX_{max}}(E, t) \right|_i \quad (5)$$

where $f_p(E)$, $f_{He}(E)$, $f_N(E)$ and $f_{Fe}(E)$ are the fractions of proton, Helium, Nitrogen and Iron events respectively, and $N(E)$ is the total number of events. The fractions f_p , f_{He} , f_N and f_{Fe} are all correlated. Furthermore, the range of allowed values is not always $[0, 1]$. This range changes depending on the values of the other fractions. For example, if f_p were 0.9, the allowed range for any of the other fractions would be $[0, 0.1]$. In order to avoid changing the fraction limits in an iterative way, we have expressed the fractions f_p , f_{He} , f_N and f_{Fe} in terms of η_1 , η_2 and η_3 as follows:

$$\begin{aligned} f_p(E) &= \eta_1 \\ f_{He}(E) &= (1 - \eta_1)\eta_2 \\ f_N(E) &= (1 - \eta_1)(1 - \eta_2)\eta_3 \\ f_{Fe}(E) &= 1 - f_p(E) - f_{He}(E) - f_N(E) \end{aligned} \quad (6)$$

Therefore, each energy bin has a set of η_1 , η_2 and η_3 which defines the mass fractions of that energy bin. The allowed range for η_1 , η_2 and η_3 is always $[0, 1]$, consequently the mass fractions are constrained to values between 0 and 1 whilst the sum of the mass fractions equals 1. So, in practice we fit η_1 , η_2 and η_3 to determine the corresponding fractions (f_p , f_{He} , f_N , f_{Fe}).

Fig. 5 displays the $\langle X_{max} \rangle$ and $\sigma(X_{max})$ predictions of the three parameterisations for each primary. The predicted $\langle X_{max} \rangle$ separation of each adjacent mass component (eg. proton vs. helium, helium vs. nitrogen) within a parameterisation is approximately 30 g/cm^2 to 40 g/cm^2 . The predicted $\sigma(X_{max})$ of the primaries is much larger for the QGSJetII-04 and Sibyll2.3 parameterisations than the Epos-LHC parameterisation.

B. Validation of the parameterisation

Fig. 6 displays the mass composition results of fitting the mass fractions using our Epos-LHC, QGSJetII-04 or Sibyll2.3 X_{max} parameterisations and the X_{max} data measured by the Pierre Auger Observatory fluorescence detector (FD) [9]. The fits took into account the detector resolution and acceptance. The mass composition obtained using our X_{max} parameterisations are consistent with the Auger analysis of the 2014 FD X_{max} data set [10], where X_{max} distribution templates from hadronic interaction models were compared to the data. The compatibility of our results with the 2014 Auger analysis validates the accuracy of our X_{max} parameterisations.

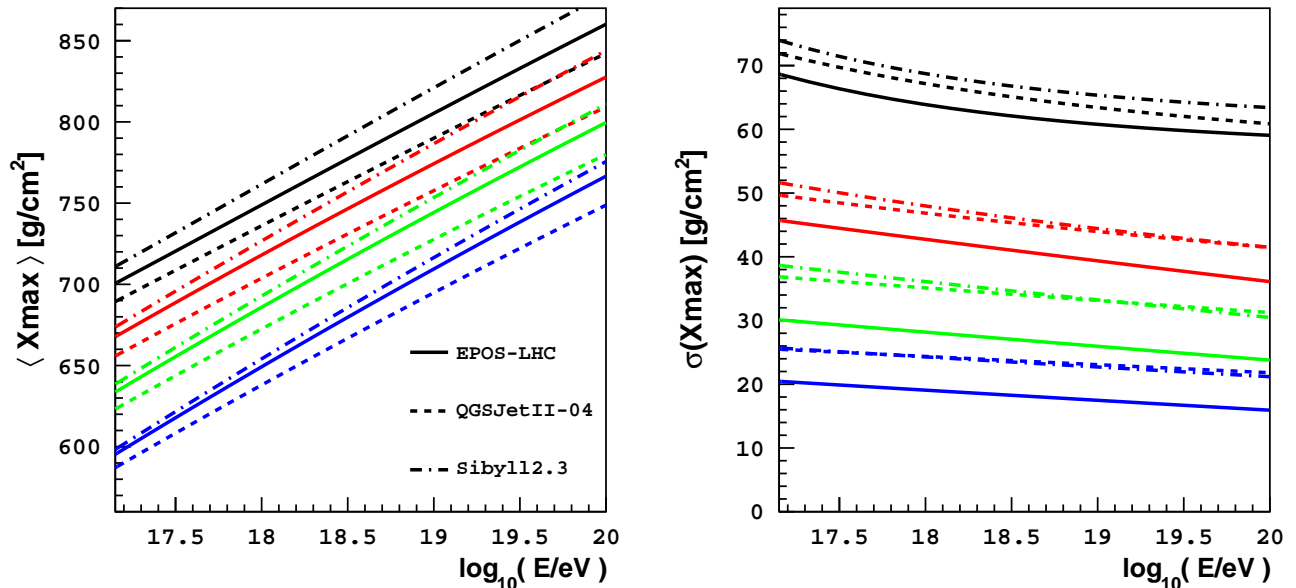


FIG. 5: The $\langle X_{\max} \rangle$ and $\sigma(X_{\max})$ predictions of the Epos-LHC, QGSJetII-04 and Sibyll2.3 X_{\max} parameterisations for proton (black), helium (red), nitrogen (green) and iron (blue).

III. METHOD

The parameters of Equation (5) are fitted to energy binned X_{\max} distributions. The coefficients of Equation (2) shown in Appendix C were obtained with a global fit which included all energy bins.

When fitting (the X_{\max} distribution data) for the mass fraction parameters using our Epos-LHC, QGSJetII-04 or Sibyll2.3 parameterisation with the coefficients fixed (as in Fig. 6), the resulting mass composition reflects the characteristics of the corresponding hadronic model. Therefore, the estimated composition depends on which hadronic model is used. Additionally, the mass composition fitted to each energy bin is independent of the mass composition fitted to other energy bins. However, by including some of the coefficients shown in Appendix C in the fit, in addition to the mass composition fractions, the mass composition obtained has a reduced dependence on the hadronic interaction model assumed. In this alternative case the mass composition fitted at each energy bin has some dependence with the fits at other energy bins. This is because the fitted coefficients (from the X_{\max} parameterisation) are fitted using all energy bins, while in the first case these coefficients were fixed.

In principle, if we were able to use the Auger X_{\max} data to perform a global fit of the mass composition and all of the coefficients from Equation (2), the resulting composition would be independent of the hadronic models, depending only on the assumed functional forms of the equations. However, the degeneracy between the fitted mass fractions and the coefficients makes it impossible to unambiguously constrain all of these parameters (i.e.

the solution would be degenerate). Therefore, we need to identify which coefficients are most relevant for interpreting the mass composition, and evaluate whether we can unambiguously fit these coefficients and the mass composition. One way to identify which coefficients to include in a global fit is to compare the values of t_0 , σ and λ between different models. This comparison will identify the parameters that are well or poorly constrained by our current knowledge of the high energy hadronic interaction physics.

Figs. 7, 8 and 9 illustrates the t_0 , σ and λ difference between the Epos-LHC, QGSJetII-04 and Sibyll2.3 parameterisations at some energy and mass. The differences as a function of energy are relatively small. For example, the slope of Δt_0 as a function of energy is less than $\sim 5 \text{ g/cm}^2$ /energy-decade, which is small compared with an elongation rate of 60 g/cm^2 /energy-decade. We have also verified that the separation between different primaries in the t_0 , σ and λ space is similar for the three tested models. The main differences between our Epos-LHC, QGSJetII-04 and Sibyll2.3 X_{\max} parameterisations are the normalisation of t_0 and σ . The difference in the normalization of λ is not negligible, but it has little impact on the mass composition interpretation. Therefore, when including $t_{0\text{norm}}$ and σ_{norm} in the global fit, we should obtain a similar interpretation of the mass composition with either the Epos-LHC, QGSJetII-04 or Sibyll2.3 X_{\max} distribution parameterisation. We choose to fit $t_{0\text{norm}}$ and σ_{norm} in the following way:

- $t_{0\text{norm}}$ is fitted such that the absolute values of $t_{0\text{norm}}$ for each primary change by the same amount. Therefore, the difference in $t_{0\text{norm}}$ between pri-

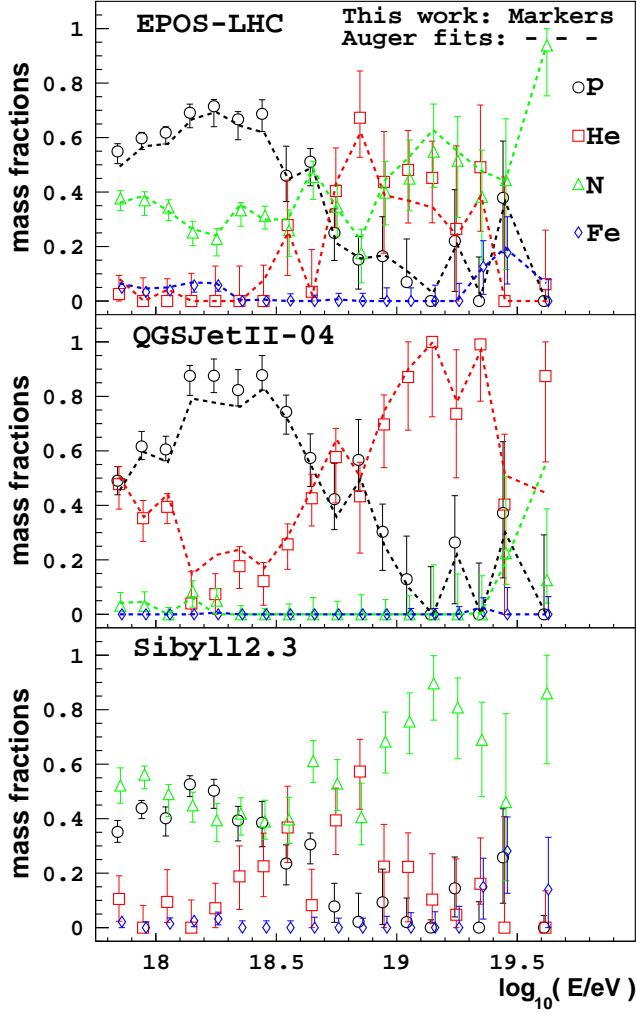


FIG. 6: Fitting only the mass fractions of our parameterisations to FD X_{\max} data measured by the Pierre Auger Observatory. The error bars represent the statistical error of the fits. Included is the mass composition results for each hadronic model from the Pierre Auger Observatory analysis (labelled ‘Auger fits’). [10].

maries is conserved.

- σ_{norm} is fitted such that the ratio of σ between primaries remains similar to the initial ratio over the energy range (differences in C between primaries prevents the exact conservation of the initial ratio). Therefore, if σ_{norm} for protons changes by Δ , σ_{norm} for other primaries will change by Δ multiplied by the initial average ratio of σ between that primary and proton.

Fitting $t_{0\text{norm}}$ and σ_{norm} in this way assumes the hadronic models are correctly predicting the separation

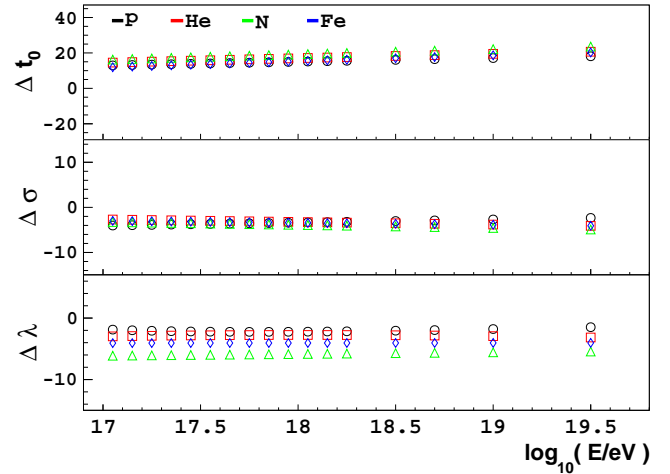


FIG. 7: Epos-LHC shape parameter value minus QGSJetII-04 shape parameter value for some mass and energy.

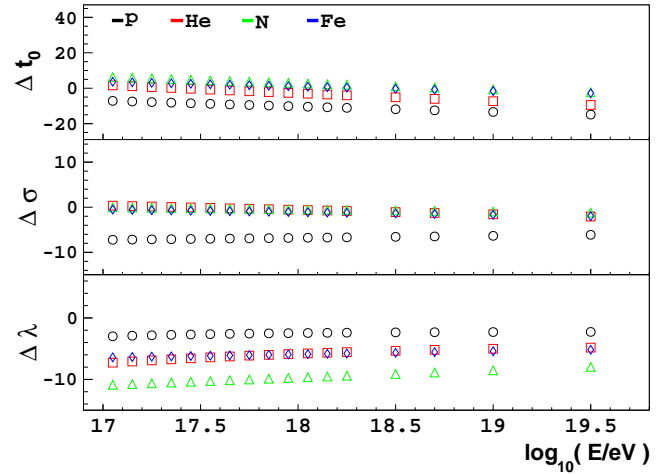


FIG. 8: Epos-LHC shape parameter value minus Sibyll2.3 shape parameter value for some mass and energy.

in t_0 between different species, and the ratio of σ between different species, over the fitted energy range.

In Equation (2), the values of the shape parameters for Helium, Nitrogen and Iron can be expressed in terms of the corresponding values for protons, therefore fitting $t_{0\text{norm}}$ and σ_{norm} in the way described above can be implemented by simply fitting $t_{0\text{norm}}$ and σ_{norm} for protons.

In order to avoid unphysical fit results, we constrain the possible fitted values for $t_{0\text{norm}}$ and σ_{norm} . These constraints are significantly wider than the separation between the Epos-LHC, QGSJetII-04 and Sibyll2.3 X_{\max} parameterisation predictions for these coefficients. The predicted value of $t_{0\text{norm}}$ for protons according to Epos-LHC is $\sim 703 \text{ g/cm}^2$, according to QGSJetII-04 is $\sim 688 \text{ g/cm}^2$, and according to Sibyll2.3 is $\sim 714 \text{ g/cm}^2$. The minimum and maximum limits of $t_{0\text{norm}}$ for pro-

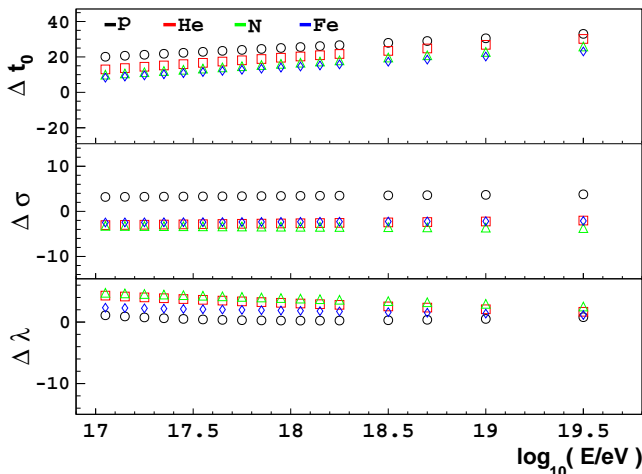


FIG. 9: Sibyll2.3 shape parameter value minus QGSJetII-04 shape parameter value for some mass and energy.

tons are set to 670 g/cm^2 and 765 g/cm^2 respectively. The predicted value of σ_{norm} for protons according to Epos-LHC, QGSJetII-04 and Sibyll2.3 is $\sim 22 \text{ g/cm}^2$, $\sim 25 \text{ g/cm}^2$ and $\sim 28 \text{ g/cm}^2$ respectively. The minimum and maximum limits of σ_{norm} for protons are set to 5 g/cm^2 and 55 g/cm^2 respectively.

With a suitable shift in $t_{0,\text{norm}}$ and σ_{norm} , many primary mixtures which produce a fairly smooth total distribution can be fitted well with a single dominant distribution, instead of a sum of distributions. On the other hand, a distribution dominated by a single primary can be well fitted by a balanced mixture of distributions when $t_{0,\text{norm}}$ and σ_{norm} are shifted appropriately. It is common that X_{max} distributions can be fitted with a value of $t_{0,\text{norm}}$ for protons much larger than the true $t_{0,\text{norm}}$ of the distributions, which results in the primary mass of the events being overestimated (i.e. biased towards heavier masses). Therefore, it is important that appropriate shape coefficient limits are chosen.

We have evaluated the performance of fitting $t_{0,\text{norm}}$ and σ_{norm} in addition to the mass fractions using simulated X_{max} distributions of a known composition (see details in Sec. IV). Provided there is enough dispersion of masses in the data, it is possible to fit with good accuracy, $t_{0,\text{norm}}$, σ_{norm} and the corresponding abundance (fractions) of p, He, N and Fe. An important achievement from including $t_{0,\text{norm}}$ and σ_{norm} in the fit is that the mass composition interpretation becomes consistent whether using the predicted Epos-LHC, QGSJetII-04 or Sibyll2.3 parameterisation.

The requirement of a large dispersion of masses is evaluated over the entire energy range. For example, a data set consisting of a pure proton composition at higher energies can be fitted, provided that at lower energies we have populations consisting of other primaries. If the statistics or mass dispersion were not large enough, there would be some degeneracy in the fit between the mass

fractions and $t_{0,\text{norm}}$ and σ_{norm} . A greater change in the mass composition with energy improves the accuracy of the fit.

Apart from the dispersion of masses in the data, the performance of the fit depends on the intrinsic values for σ of the data. This is nature's width for the X_{max} distribution of the different primaries. The separation of the distribution modes between primaries remains unchanged in the fit, therefore primary X_{max} distributions of larger width will increase the X_{max} distribution overlap of adjacent primaries, resulting in the fit of $t_{0,\text{norm}}$, σ_{norm} and the mass composition becoming more uncertain.

We have also evaluated the performance of fitting $t_{0,\text{norm}}$, B , and σ_{norm} in addition to the mass fractions, where B defined in Equation (2) describes the change in t_0 with energy. As the predicted mass composition is particularly sensitive to the predicted values of t_0 , B is a powerful coefficient which can significantly affect the fitted mass composition. We fit B such that for each primary the value of B changes by the same amount from the initial predicted value, thus the initial predicted differences among primaries in the rate of change of t_0 with energy are conserved (identical to how $t_{0,\text{norm}}$ is fitted). Our X_{max} parameterisations have similar values for B , therefore we do not expect fits of B to yield results significantly different from the initial prediction of B when we are fitting Epos-LHC, QGSJetII-04 or Sibyll2.3 simulated X_{max} data. However, if the values of B predicted by our parameterisations are significantly incorrect for the data being fitted, considerable systematics would be introduced to the reconstructed mass composition if B remains fixed.

Data sets that can be fitted with $t_{0,\text{norm}}$ and σ_{norm} may not be accurately fitted when B is included in the fit, as fitting extra coefficients increases the degeneracy between the fitted variables. Fitting these three coefficients accurately requires a greater spread of primaries and/or statistics than fitting just $t_{0,\text{norm}}$ and σ_{norm} . The predicted value of B for protons according to Epos-LHC, QGSJetII-04 and Sibyll2.3 is $\sim 2533 \text{ g/cm}^2$, $\sim 2445 \text{ g/cm}^2$ and $\sim 2666 \text{ g/cm}^2$ respectively. With $t_{0,\text{norm}}$ normalised at $10^{18.24} \text{ eV}$, a change in B of 350 g/cm^2 corresponds to a change in t_0 at $10^{19.5} \text{ eV}$ of $\sim 10 \text{ g/cm}^2$. The fitting range limits of B for protons is 1000 g/cm^2 to 4000 g/cm^2 .

We have also considered constraining t_0 at 10^{14} eV , where the hadronic models are more reliable, and fitting B and σ_{norm} . Fitting B in this way can also provide a consistent mass fraction result between the Epos-LHC, QGSJetII-04 and Sibyll2.3 parameterisation fits of simulated X_{max} data, as the t_0 prediction of the fitted energy range adjusts in a way that is similar to the $t_{0,\text{norm}}$ fit, with the added advantage that unlike the $t_{0,\text{norm}}$ fit, the resulting fitted parameterisation of t_0 is consistent with the hadronic model predictions at lower energies. We have found that over the energy range of interest

($10^{17.8}$ eV to 10^{20} eV), fitting $t_{0,\text{norm}}$ and σ_{norm} results in a more accurate mass composition reconstruction compared to fitting B and σ_{norm} . This is because there is less degeneracy between the fitted mass fractions and shape parameters when fitting $t_{0,\text{norm}}$ and σ_{norm} . Additionally, a t_0 parameterisation constrained at $10^{18.24}$ eV describes the energy range of interest better than a t_0 parameterisation extrapolated from 10^{14} eV. If a wider energy range was being fitted, then a $t_{0,\text{norm}}$ and σ_{norm} fit would be less accurate, because the t_0 and σ parameterisations of different models do not adequately align over a wider energy range by only adjusting their normalisations. It is also important to recognise that this fit of B is restricted, as we are fixing how t_0 changes with energy, and only fitting the rate of change of the $\log_{10} \left(\frac{\log_{10} E}{\log_{10} E_0} \right)$ factor. To properly fit the slope of t_0 with energy would require the fit of a third t_0 parameter (for example, fitting B and x in $B \cdot \log_{10} \left(\frac{\log_{10} E}{\log_{10} E_0} \right)^x$, where x currently equals 1).

We have evaluated the effect of different X_{max} bin sizes and energy bin sizes on the performance of the fit. When fitting only the mass fractions, 1 g/cm^2 X_{max} binning gives marginally more accurate results than 20 g/cm^2 X_{max} binning (20 g/cm^2 is the X_{max} bin size of the Auger X_{max} distributions published in [9]). The absolute improvement in the fitted mass fractions is no greater than 3% in an energy bin. However, when fitting $t_{0,\text{norm}}$ and σ_{norm} in addition to the mass fractions, using a small X_{max} binning is more important, otherwise the chosen center of the X_{max} bins may significantly affect the fitted results, especially if the statistics are not large. The predicted separation between different primaries in $t_{0,\text{norm}}$ and σ_{norm} can be very small. For example, our Epos-LHC parameterisation predicts the difference in $t_{0,\text{norm}}$ between proton and helium is only $\sim 6 \text{ g/cm}^2$. Therefore, a 20 g/cm^2 X_{max} binning (as published in [9]) can be too coarse, and can shift the apparent $\langle X_{\text{max}} \rangle$ of the distribution, which affects the fit of $t_{0,\text{norm}}$.

Due to similar reasons, the energy bin size is also important. Energy binning that is too large can result in data from the same primary mass, but on opposite extremes of the energy bin, being evaluated as data from different primaries. This is because the separation between the predicted X_{max} distributions of different primaries is small compared to the shift in these X_{max} distributions with energy. We find that an energy binning of 0.1 in $\log_{10}(E/\text{eV})$ is reasonable.

IV. PERFORMANCE

Using CONEX v4r37, 100 X_{max} data sets were generated according to both the Epos-LHC and QGSJetII-04 hadronic interaction models for a number of different mass compositions. The data consists of 17 energy bins, of which there are 13 energy bins of a width of 0.1 in $\log_{10}(E/\text{eV})$ between 10^{17} eV and $10^{18.3}$ eV, and 4 fixed

energy bins at $10^{18.5}$ eV, $10^{18.7}$ eV, 10^{19} eV and $10^{19.5}$ eV. Each energy bin contains approximately 750 events. The binning of the simulated X_{max} distributions is 1 g/cm^2 .

We have fitted only the mass fractions (all coefficients from the X_{max} parameterisation were kept fixed) to data of a single primary generated with the same hadronic interaction model the parameterisation fitted is based on. Figs. 10 to 13 summarises the results (of these 100 fits) for the Epos-LHC hadronic model and Figs. 14 to 17 for the QGSJetII-04 model. The markers represent the medians of the fitted mass fractions, and the error bars represent the standard deviation. The results show that our X_{max} parameterisations are an accurate description of the expected X_{max} distribution of a primary according to the Epos-LHC or QGSJetII-04 hadronic interaction models. Both our Epos-LHC and QGSJetII-04 X_{max} parameterisation fits can accurately determine the mass composition of data from the same hadronic model.

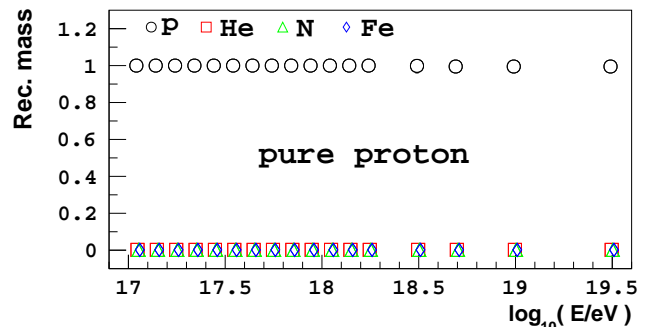


FIG. 10: Fitting only the mass fractions to mock data sets of X_{max} distributions. The data sets have been generated using the Epos-LHC model and assuming a **proton** primary composition over the whole energy range. The composition fits were performed using our X_{max} parameterisations for the Epos-LHC model predictions. ‘Rec. mass’ refers to the mass fractions fitted to the data.

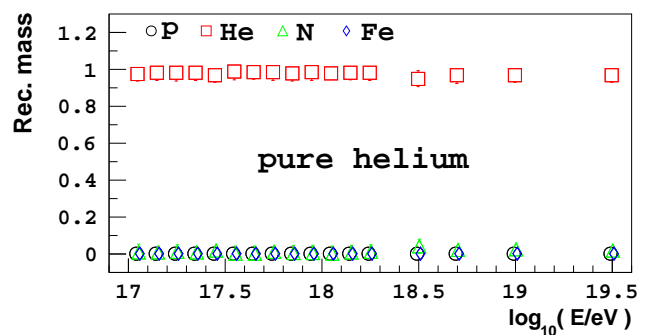


FIG. 11: Same as Fig. 10, but assuming a **Helium** primary composition over the whole energy range.

Fig. 18 to Fig. 20 summarises the results of fits to 100 X_{max} data sets with a true mass composition consisting

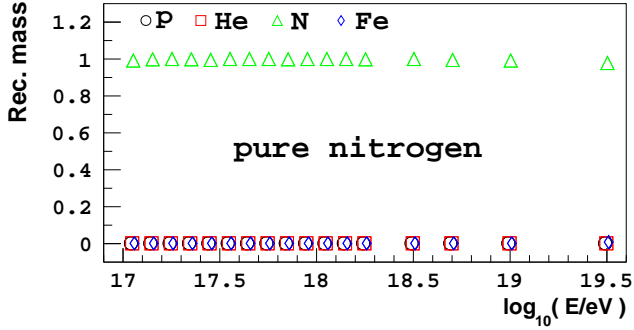


FIG. 12: Same as Fig. 10 but assuming a **Nitrogen** primary composition over the whole energy range.

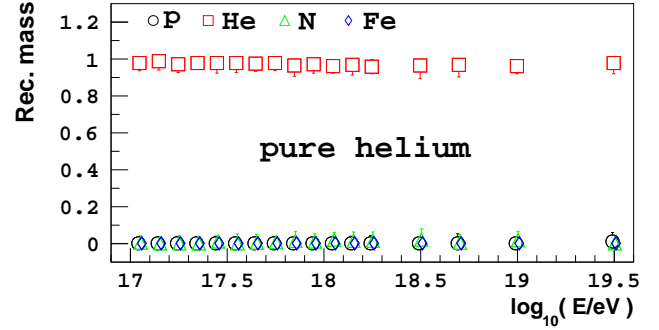


FIG. 15: Same as Fig. 14, but assuming a **Helium** primary composition over the whole energy range.

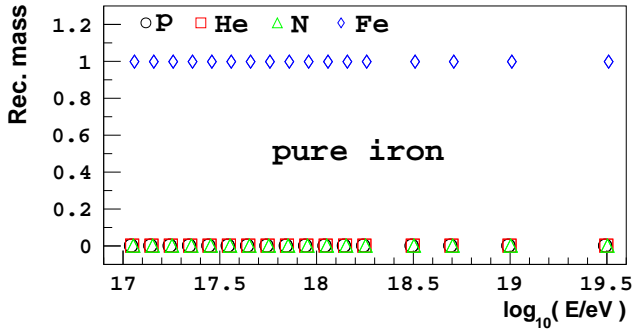


FIG. 13: Same as Fig. 10, but assuming an **Iron** primary composition over the whole energy range.

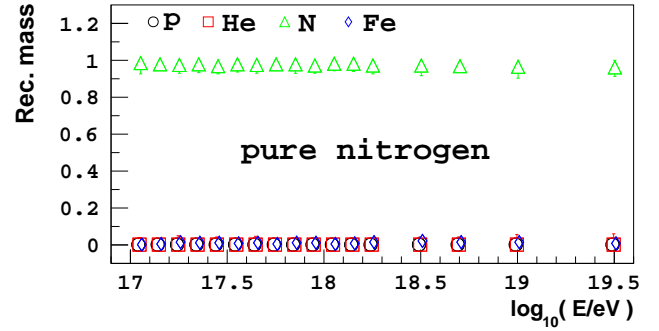


FIG. 16: Same as Fig. 14 but assuming a **Nitrogen** primary composition over the whole energy range.

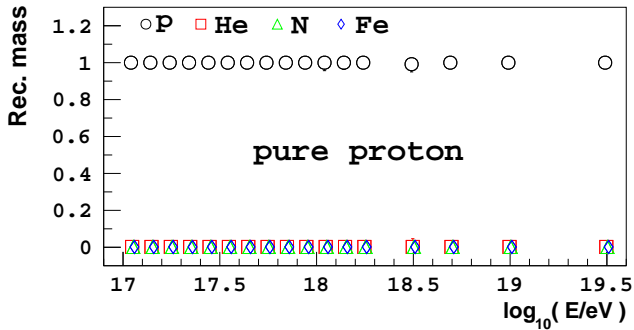


FIG. 14: Fitting only the mass fractions to mock data sets of X_{\max} distributions. The data sets have been generated using the QGSJetII-04 model and assuming a **proton** primary composition over the whole energy range. The composition fits were performed using our X_{\max} parameterisations for the QGSJetII-04 model predictions.

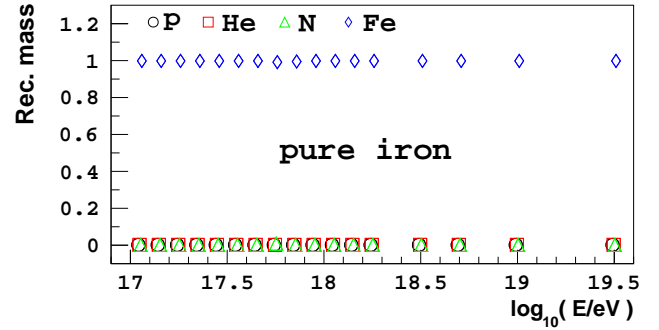


FIG. 17: Same as Fig. 14, but assuming an **Iron** primary composition over the whole energy range.

of 50% proton and helium in the first 8 energy bins, and 50% helium and nitrogen in the remaining 9 energy bins. When fitting only the mass fractions (i.e. keeping fixed the coefficients of the X_{\max} distribution parameterisation) of our parameterisations to CONEX v4r37 X_{\max} data based on the same model, the fits are able to recon-

struct the mass composition to within an absolute offset in the median of 10% from the true mass (as seen in Figs. 18 and 19).

Fig. 20 shows the results of fitting $t_{0,\text{norm}}$ and σ_{norm} , in addition to the mass fractions, of the QGSJetII-04 parameterisation to QGSJetII-04 data. These QGSJetII-04 X_{\max} distributions do not provide sufficient constraints on our fitted parameterisation, resulting in a mass composition reconstruction that does not resemble the true mass composition. In order to successfully fit $t_{0,\text{norm}}$ and σ_{norm} to data of a similar distribution, a wider range of

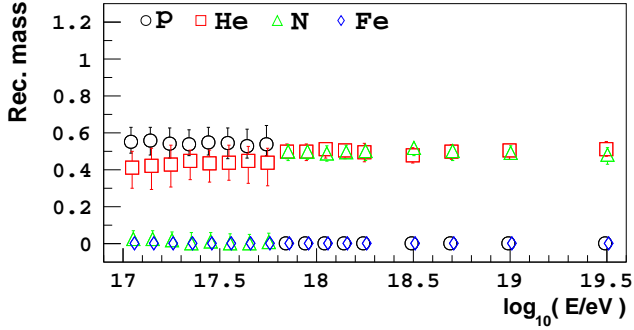


FIG. 18: Fitting only the mass fractions of our Epos-LHC parameterisation to Epos-LHC X_{\max} data.

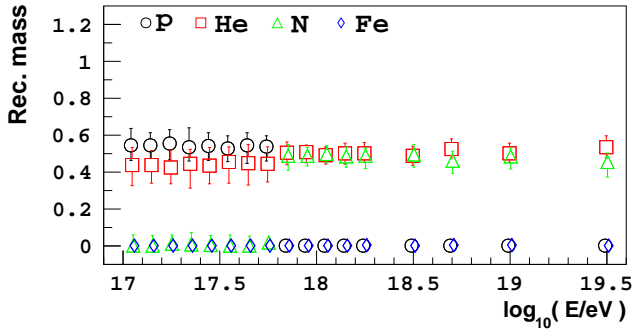


FIG. 19: Fitting only the mass fractions of our QGSJetII-04 parameterisation to QGSJetII-04 X_{\max} data.

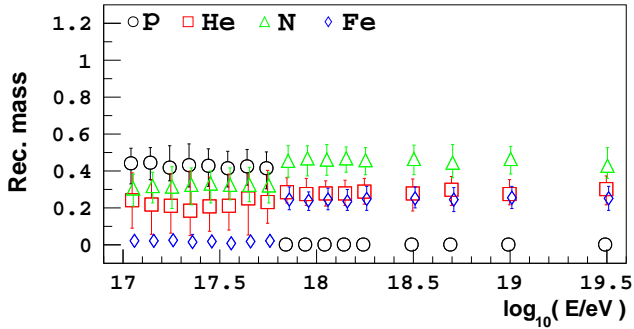


FIG. 20: Fitting $t_{0\text{norm}}$, σ_{norm} and the mass fractions of our QGSJetII-04 parameterisation to QGSJetII-04 X_{\max} data.

primary masses over the energy range of the data is required (wider than the one in the given example). For example, in Fig. 21 we have increased the range of primary masses by replacing helium with iron in the last energy bin. The resulting fit of the mass fractions (with $t_{0\text{norm}}$ and σ_{norm} also fitted) have an absolute offset in the median of less than $\sim 15\%$ from the true values, which is comparable to a fit of only the mass fractions to data of a similar composition.

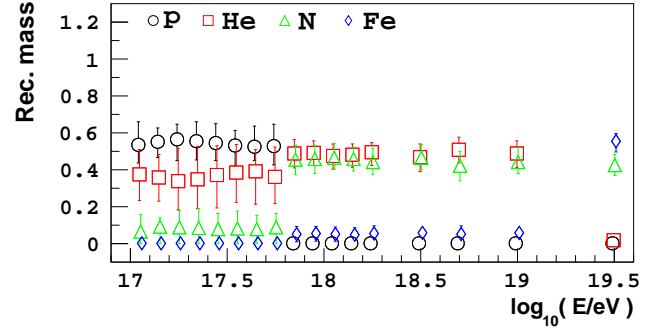


FIG. 21: Fitting $t_{0\text{norm}}$, σ_{norm} and the mass fractions of our QGSJetII-04 parameterisation to QGSJetII-04 X_{\max} data. Helium has been replaced by Iron in the last energy bin to increase the mass dispersion.

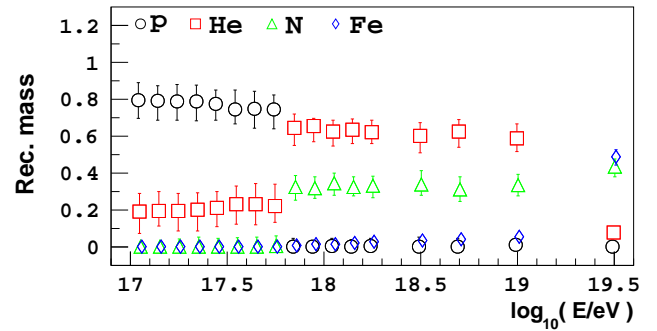


FIG. 22: Fitting $t_{0\text{norm}}$, σ_{norm} and the mass fractions of our Epos-LHC parameterisation to QGSJetII-04 X_{\max} data. Helium has been replaced by Iron in the last energy bin to increase the mass dispersion.

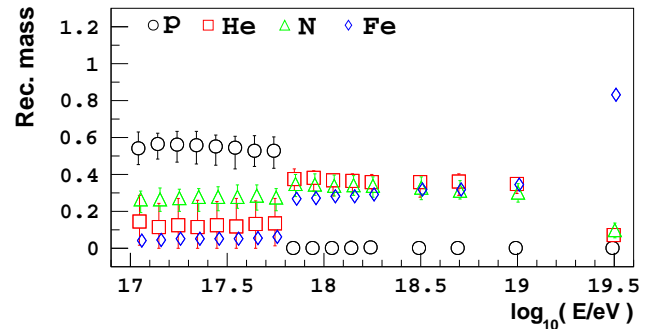


FIG. 23: Fitting only the mass fractions (i.e. $t_{0\text{norm}}$ and σ_{norm} are kept fixed) of our Epos-LHC parameterisation to QGSJetII-04 X_{\max} data. Compare this Fig. with Fig. 22 where $t_{0\text{norm}}$ and σ_{norm} were included in the fit.

A. Fitting data originating from a different model.

Compare Fig. 22 with Fig. 23, which shows the composition fits when using the Epos-LHC parameterisation to fit QGSJetII-04 data, with $t_{0\text{norm}}$ and σ_{norm} fitted in

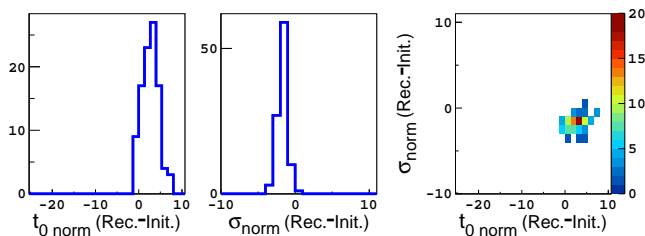


FIG. 24: Change in $t_{0\text{norm}}$ and σ_{norm} for protons from the fits in Fig. 21.

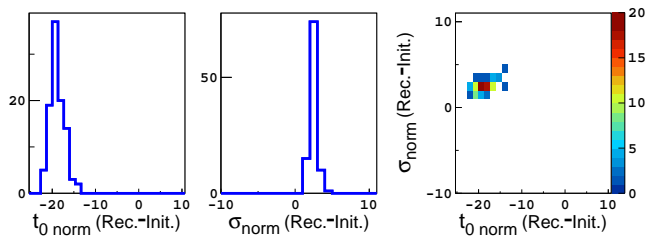


FIG. 25: Change in $t_{0\text{norm}}$ and σ_{norm} for protons from the fits in Fig. 22.

the former, and $t_{0\text{norm}}$ and σ_{norm} fixed in the latter. Fitting these two coefficients is enough to result in a reconstructed mass much closer to the true mass, despite the fitted data originating from a different model. By fitting $t_{0\text{norm}}$ and σ_{norm} , there is no longer a significant iron component where there should only be 50% helium and nitrogen, and in the 50% proton and helium range there is no longer a fitted nitrogen component larger than the helium fraction.

Figs. 24 and 25 show the difference between the fitted values and initial values of $t_{0\text{norm}}$ and σ_{norm} (and their correlation) when fitted to the data with iron added in the last energy bin. Fig. 24 displays the results of fitting QGSJetII-04 data with our QGSJetII-04 parameterisation, and as expected the difference between the reconstructed and initial values of our coefficients is minimal. Fig. 25 displays the results of fitting the same QGSJetII-04 data with our Epos-LHC parameterisation (the reconstructed mass is shown in Fig. 22), and we see that $t_{0\text{norm}}$ and σ_{norm} are shifted towards the QGSJetII-04 values for these coefficients. The initial Epos-LHC proton $t_{0\text{norm}}$ and σ_{norm} values are $\sim 703 \text{ g/cm}^2$ and $\sim 22 \text{ g/cm}^2$ respectively, while the initial QGSJetII-04 proton $t_{0\text{norm}}$ and σ_{norm} values (and therefore the approximate values of the QGSJetII-04 MC data) are $\sim 688 \text{ g/cm}^2$ and $\sim 25 \text{ g/cm}^2$ respectively.

Notice that in Fig. 18 to Fig. 22 the bins containing a helium and nitrogen mix are reconstructed better than the bins containing a proton and helium mix. Proton and helium distributions are harder to reconstruct due to their wider spread and their larger overlap. A wider spread means that for a given number of events, less events will populate individual X_{max} bins. Therefore, proton and helium fits have larger statistical uncertain-

ties. Additionally, the X_{max} parameterisations for lighter masses do not describe the CONEX v4r37 Epos-LHC and QGSJetII-04 simulated data as accurately. Fig. 58 in Appendix A illustrates that as the primary mass of the distribution increases, the X_{max} parameterisations reproduce the true $\langle X_{\text{max}} \rangle$ and $\sigma(X_{\text{max}})$ of the distributions with better accuracy. Appendix A shows that for proton and helium data especially, the fits of Equation (1) to MC data of either hadronic model tend to overestimate the number of events at the mode of the distribution. When fitting mixes of protons and helium, our fits tend to have a reconstruction bias towards protons.

As the absolute separation between σ for different primaries is similar in the Epos-LHC and QGSJetII-04 parameterisations (like t_0), marginally better results would be obtained in Fig. 22 if instead of fitting σ_{norm} such that the initial ratios of σ among primaries are conserved, σ_{norm} was fitted such that the initial separation between σ_{norm} among primaries was conserved (like $t_{0\text{norm}}$). However, conserving the initial ratios of σ is the more physical approach, because if σ_{norm} for protons changes by 10 g/cm^2 , we would not expect that σ_{norm} for iron would also change by 10 g/cm^2 . Additionally, nature does not necessarily conform to the Epos-LHC or QGSJetII-04 predictions of the absolute separation of σ_{norm} among primaries.

V. $t_{0\text{norm}}$ AND σ_{norm} PARAMETER SPACE SCAN OF THE AUGER FD X_{max} DATA

Fig. 26 shows the minimised Poisson log likelihood space of the mass fraction fit of a parameterisation to Auger FD X_{max} data, where $t_{0\text{norm}}$ and σ_{norm} have been fixed to some particular value (indicated by the x and y axes). The z-axis shows the difference between the minimised probability for some value of $t_{0\text{norm}}$ and σ_{norm} , and the absolute minimised probability obtained from the $t_{0\text{norm}}$ and σ_{norm} values which best fitted the data for a particular parameterisation. A difference of 1 in the minimised Poisson log likelihood corresponds to 1σ . The absolute minima of the Epos-LHC and QGSJetII-04 fits to the Auger FD data correspond to a similar value of $t_{0\text{norm}}$ for protons, whereas the absolute minimum of the Sibyll2.3 fit is located at a significantly larger value of $t_{0\text{norm}}$ for protons. Between the three fitted parameterisations, when estimating the heavier nuclei $t_{0\text{norm}}$ values there is more similarity. This is because the separation between the proton t_0 prediction and heavier nuclei is larger in the Sibyll2.3 parameterisation than Epos-LHC or QGSJetII-04 (see Figs. 7, 8 and 9). This is also true for σ .

These scans show that the fits of the Auger FD X_{max} data performed in Section VII did not become stuck in a local minimum. The scans can also reveal secondary solutions which are not as deep as the deepest minimum.

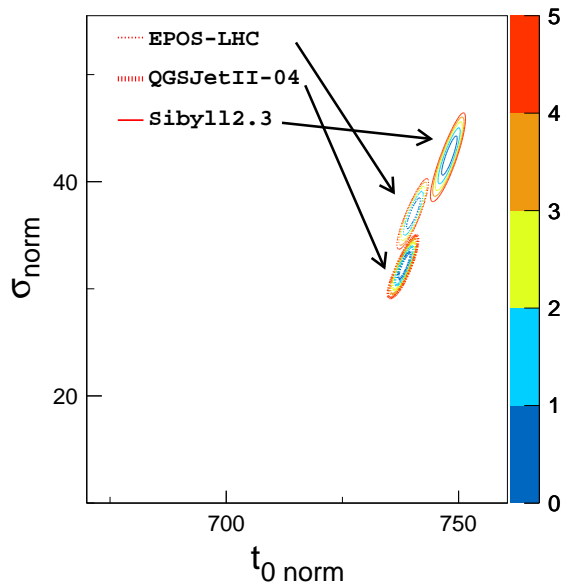


FIG. 26: The $t_{0\text{norm}}$ and σ_{norm} parameter space scan over the Auger FD X_{max} data. For each model parameterisation, at specific values of $t_{0\text{norm}}$ and σ_{norm} , the mass fractions are fitted to the data, and the first 5σ contours of the minimised Poisson log likelihood are shown. The scanned shape coefficient values for proton are shown. The coefficient values of the heavier nuclei change (relative to protons) in the way the shape coefficient would be fitted, outlined in Section III.

VI. EVALUATING THE FIT PERFORMANCE FOR A MASS COMPOSITION CONSISTENT WITH THE AUGER RESULTS

The performance of fitting $t_{0\text{norm}}$, σ_{norm} and the mass fractions of our parameterisations to the Auger FD X_{max} data is evaluated by fitting mock X_{max} data sets that resemble the Auger FD X_{max} distributions. This was achieved by fitting $t_{0\text{norm}}$, σ_{norm} and the mass fractions of a particular parameterisation to the Auger FD X_{max} data, and then using this fitted parameterisation to generate the mock data sets. Appendix C displays the $t_{0\text{norm}}$ and σ_{norm} values fitted to the Auger data, values which correspond to the absolute minima found from the scans in Section V. These mock data sets have a true mass composition which is defined by the parameterisation used to generate them, therefore we can evaluate the ability of our $t_{0\text{norm}}$, σ_{norm} and mass fraction fit to accurately reconstruct the true mass fractions. The binning of the mock Auger X_{max} distributions is 20 g/cm^2 .

The measured FD X_{max} distributions are broadened by the X_{max} resolution of the detector, and are affected by the detector acceptance, therefore the mock X_{max} data generated from the fitted parameterisation are convolved with the same detector effects. The X_{max} resolution and acceptance of the Auger data is taken into account when

fitting this mock Auger X_{max} data. Our mock X_{max} distributions and the X_{max} distributions measured by Auger are treated with exactly the same approach.

A. Fitting $t_{0\text{norm}}$, σ_{norm} and the mass fractions

Figs. 27, 28 and 29 display the mass composition results from fitting the mass fractions, $t_{0\text{norm}}$ and σ_{norm} of either the Epos-LHC, QGSJetII-04 or Sibyll2.3 parameterisations respectively, to 100 data sets generated from the parameterisation which resulted when the mass fractions, $t_{0\text{norm}}$ and σ_{norm} of the **Epos-LHC** parameterisation were fitted to Auger FD X_{max} data (as will be shown in Section VII). The true mass composition of the mock data is therefore the mass composition which resulted from the Epos-LHC fit to the Auger FD X_{max} data. Figs. 30, 31 and 32 display the fitted proton values of $t_{0\text{norm}}$ and σ_{norm} relative to the original values of the model applied, compared to the change required to match the true proton values of the mock data. The red lines indicate the mock data input values and the blue histograms are the reconstructed values. The correlations between the reconstructed $t_{0\text{norm}}$ and σ_{norm} are also shown in Figs. 30, 31 and 32. There are no reconstruction systematics when using the Epos-LHC parameterisation to fit Epos-LHC generated data (Fig. 30), but there are some systematics when using the QGSJetII-04 or Sibyll2.3 parameterisations to fit Epos-LHC generated data (Figs. 31 and 32). These systematics in $t_{0\text{norm}}$ and σ_{norm} translate into relative small systematics of the reconstructed mass fractions (as seen in Figs. 28 and 29).

Figs. 28 and 31 show that despite the differences between the Epos-LHC and QGSJetII-04 parameterisations (which are not limited to different $t_{0\text{norm}}$ and σ_{norm} predictions), by allowing $t_{0\text{norm}}$ and σ_{norm} of the QGSJetII-04 X_{max} parameterisation to be fitted to mock data based on the Epos-LHC parameterisation, the true mass fractions are reconstructed with an overall accuracy comparable to the Epos-LHC fits of Epos-LHC data. The absolute offsets in the median mass fractions from the true mass are less than 10% in most energy bins. This demonstrates that fitting $t_{0\text{norm}}$ and σ_{norm} significantly reduces the differences between the Epos-LHC and QGSJetII-04 X_{max} parameterisations. As we are fitting the QGSJetII-04 parameterisation to mock data based on the Epos-LHC parameterisation, we do not expect the average fitted values of $t_{0\text{norm}}$ and σ_{norm} to be centred on the red lines even if no systematic offset was present in the mass fractions reconstruction. This is because the separation of these coefficients between masses differs between the Epos-LHC and QGSJetII-04 parameterisations, thus if the fitted QGSJetII-04 value of $t_{0\text{norm}}$ for protons was equal to the Epos-LHC value of $t_{0\text{norm}}$ for protons, the accordingly adjusted $t_{0\text{norm}}$ values of other masses would differ between these parameterisations.

The mass composition reconstruction accuracy of the Epos-LHC fit to Epos-LHC based data changes less with

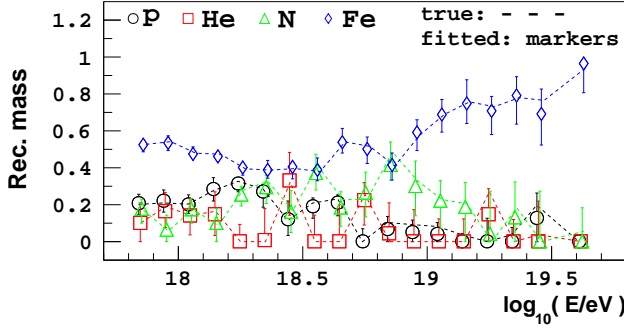


FIG. 27: Epos-LHC fit of X_{\max} data generated from the Epos-LHC parameterisation fit of Auger data.

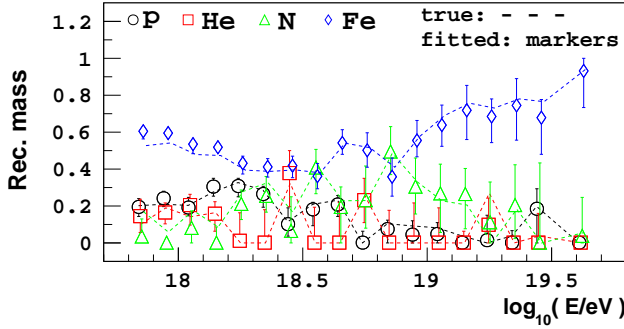


FIG. 28: QGSJetII-04 fit of X_{\max} data generated from the Epos-LHC parameterisation fit of Auger data.

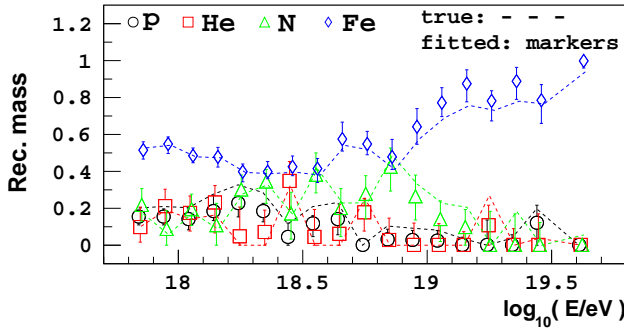


FIG. 29: Sibyll2.3 fit of X_{\max} data generated from the Epos-LHC parameterisation fit of Auger data.

energy than the accuracy of the QGSJetII-04 fit to the Epos-LHC data. This is because the Epos-LHC t_0 parameterisation fit to the Epos-LHC based data is offset by a constant value at all energies from the true t_0 of the mock data, whereas the difference between the fitted QGSJetII-04 t_0 parameterisation and the true t_0 of the mock data (based on Epos-LHC) changes with energy.

Fig. 29 shows the Sibyll2.3 fit to the Epos-LHC data results in a reconstructed mass that is very representative of the true mass, but this mass reconstruction is not as accurate as the Epos-LHC and QGSJetII-04

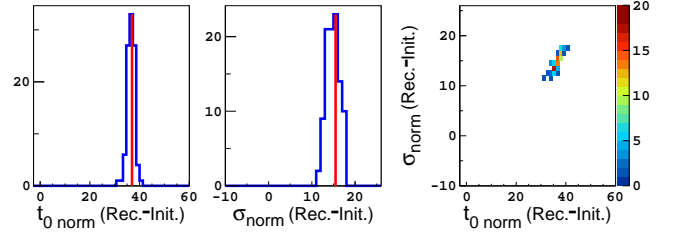


FIG. 30: Change in $t_{0\text{norm}}$ and σ_{norm} for protons from the fits in Fig. 27.

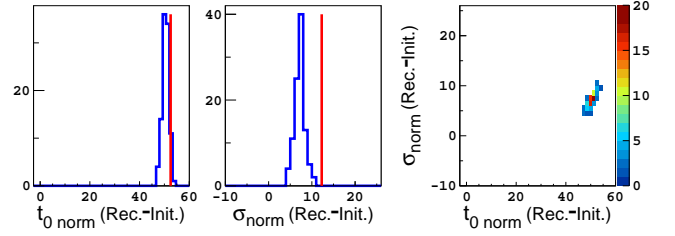


FIG. 31: Change in $t_{0\text{norm}}$ and σ_{norm} for protons from the fits in Fig. 28.

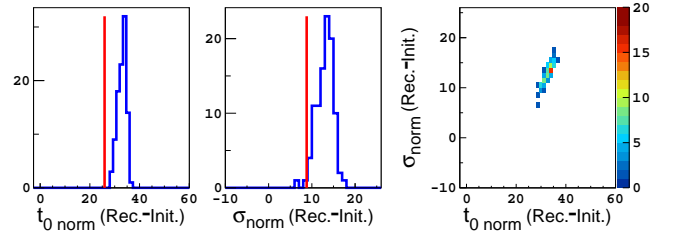


FIG. 32: Change in $t_{0\text{norm}}$ and σ_{norm} for protons from the fits in Fig. 29.

fits to this data. This is because a $t_{0\text{norm}}$ and σ_{norm} shift of the Sibyll2.3 parameterisation does not align the Sibyll2.3 t_0 and σ parameterisations with the Epos-LHC (or QGSJetII-04) descriptions as adequately as the Epos-LHC or QGSJetII-04 descriptions can be aligned with each other (compare Figs. 7, 8 and 9). Larger differences in the λ Sibyll2.3 parameterisation relative to the other parameterisations further hinders an accurate mass reconstruction of data based on these other parameterisations.

Similar to the earlier figures presented, Figs. 33, 34 and 35 display the mass composition results from fitting the mass fractions, $t_{0\text{norm}}$ and σ_{norm} of either the Epos-LHC, QGSJetII-04 or Sibyll2.3 parameterisations respectively, to 100 data sets generated from the parameterisation which resulted when the mass fractions, $t_{0\text{norm}}$ and σ_{norm} of the **QGSJetII-04** parameterisation were fitted to Auger FD X_{\max} data. The true mass composition of the mock data is the mass composition from this QGSJetII-04 fit to the Auger FD X_{\max} data. The QGSJetII-04 based mock X_{\max} distributions will be slightly different to the Epos-LHC based mock distributions, because the X_{\max} parameterisations do not

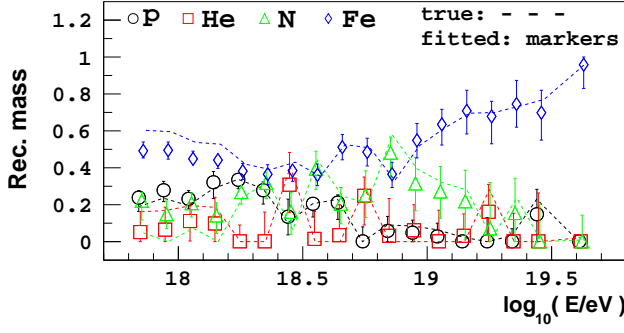


FIG. 33: Epos-LHC fit of X_{\max} data generated from the QGSJetII-04 parameterisation fit of Auger data.

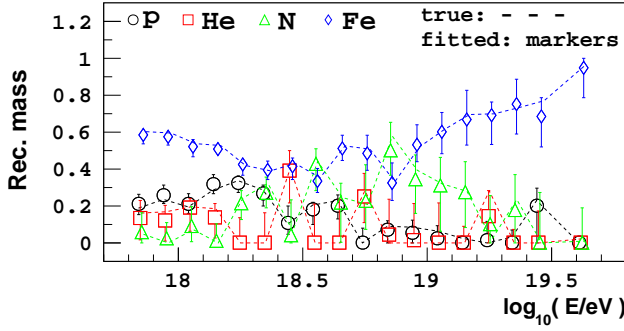


FIG. 34: QGSJetII-04 fit of X_{\max} data generated from the QGSJetII-04 parameterisation fit of Auger data.

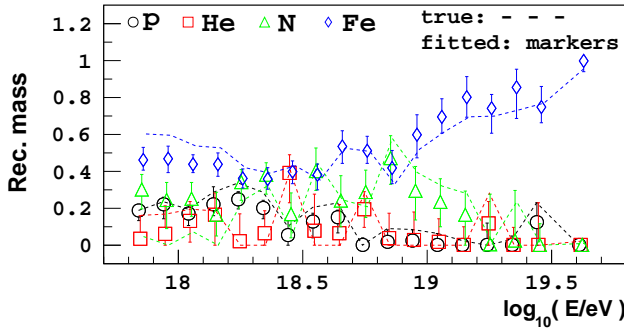


FIG. 35: Sibyll2.3 fit of X_{\max} data generated from the QGSJetII-04 parameterisation fit of Auger data.

perfectly fit the Auger data, and the respective parameterisations consist of differences which can not be compensated for by an appropriate $t_{0\text{norm}}$ and σ_{norm} shift. Figs. 36, 37 and 38 display the fitted values of $t_{0\text{norm}}$ and σ_{norm} for the Epos-LHC, QGSJetII-04 or Sibyll2.3 fits respectively to the QGSJetII-04 based data.

The fits to QGSJetII-04 based mock data produce similar results to the fits of Epos-LHC based mock data. The mass fraction, $t_{0\text{norm}}$ and σ_{norm} fit of the Epos-LHC parameterisation to QGSJetII-04 based mock data reconstructs the mass composition above $10^{18.2}$ eV with an

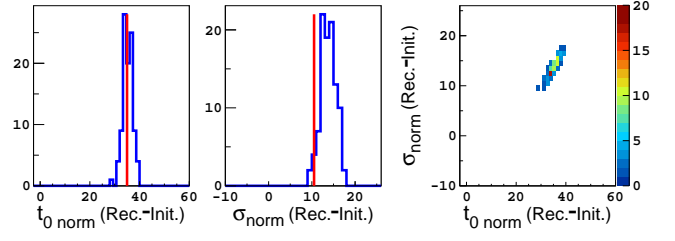


FIG. 36: Change in $t_{0\text{norm}}$ and σ_{norm} for protons from the fits in Fig. 33.

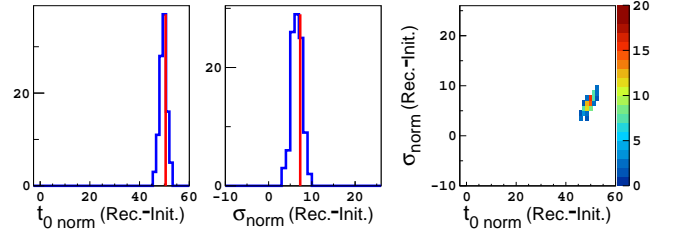


FIG. 37: Change in $t_{0\text{norm}}$ and σ_{norm} for protons from the fits in Fig. 34.

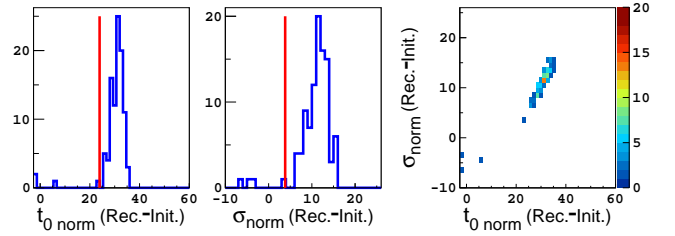


FIG. 38: Change in $t_{0\text{norm}}$ and σ_{norm} for protons from the fits in Fig. 35.

accuracy almost as good as the QGSJetII-04 parameterisation fit to the same data. For both the Epos-LHC and QGSJetII-04 fits, the absolute offsets in the median mass fractions from the true mass are less than 10% in most energy bins. As noted before, due to the differences between the Epos-LHC and QGSJetII-04 t_0 descriptions as a function of energy, the mass reconstruction accuracy of the Epos-LHC fit varies more with energy than the QGSJetII-04 fit. Again the Sibyll2.3 fit, in this case to QGSJetII-04 based data, does not reconstruct the mass composition as accurately as the Epos-LHC or QGSJetII-04 fits.

Figs. 39, 40 and 41 display the mass composition results from fitting the mass fractions, $t_{0\text{norm}}$ and σ_{norm} of either the Epos-LHC, QGSJetII-04 or Sibyll2.3 parameterisations respectively, to 100 data sets generated from the parameterisation which resulted when the mass fractions, $t_{0\text{norm}}$ and σ_{norm} of the **Sibyll2.3** parameterisation were fitted to Auger FD X_{\max} data. Figs. 42, 43 and 44 display the respective $t_{0\text{norm}}$ and σ_{norm} from these fits. The Epos-LHC and QGSJetII-04 fits to the Sibyll2.3 based data do not reconstruct the true mass composition as accurately as the Sibyll2.3 fit, but they do accurately

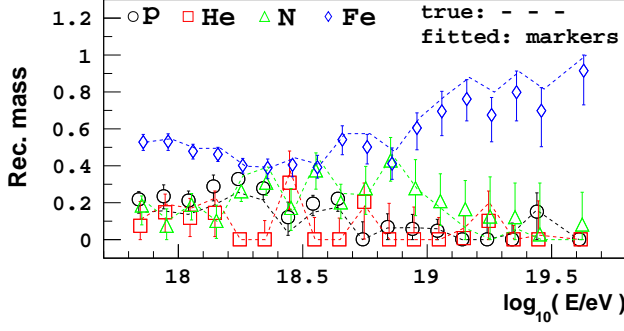


FIG. 39: Epos-LHC fit of X_{\max} data generated from the Sibyll2.3 parameterisation fit of Auger data.

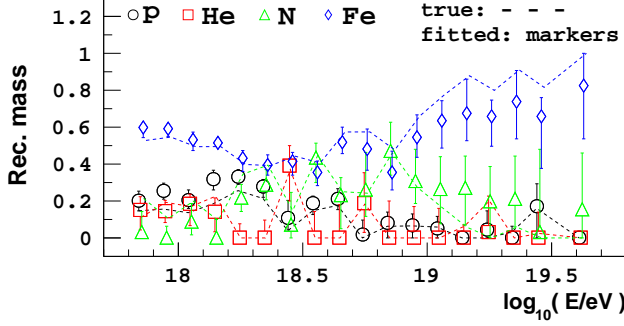


FIG. 40: QGSJetII-04 fit of X_{\max} data generated from the Sibyll2.3 parameterisation fit of Auger data.

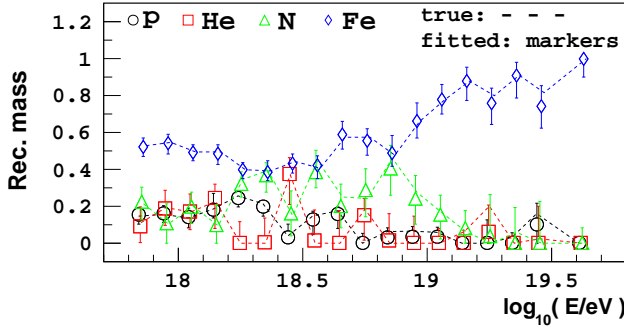


FIG. 41: Sibyll2.3 fit of X_{\max} data generated from the Sibyll2.3 parameterisation fit of Auger data.

represent the general transition of the mass composition. The Sibyll2.3 fit to Sibyll2.3 based data (see Figs. 41 and 44) results in absolute offsets in the median mass fractions from the true mass of less than 10%.

The data fitted in this section sufficiently constrains the fitted values of $t_{0\text{norm}}$ and σ_{norm} , regardless of the parameterisation fitted. If different populations of $t_{0\text{norm}}$ and σ_{norm} were present in a histogram plot, it would indicate the data is unable to adequately constrain the fit, due to the degeneracy between the fitted shape coefficients and the mass fractions.

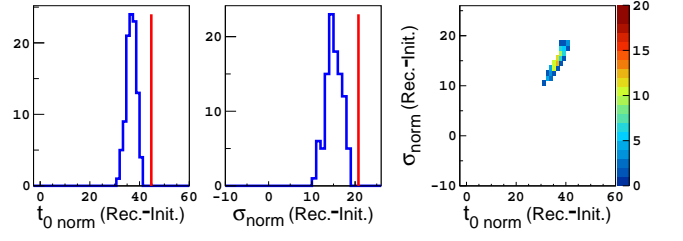


FIG. 42: Change in $t_{0\text{norm}}$ and σ_{norm} for protons from the fits in Fig. 39.

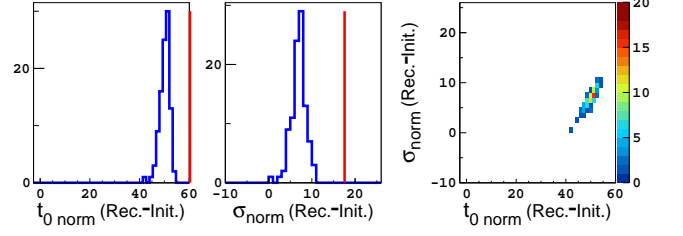


FIG. 43: Change in $t_{0\text{norm}}$ and σ_{norm} for protons from the fits in Fig. 40.

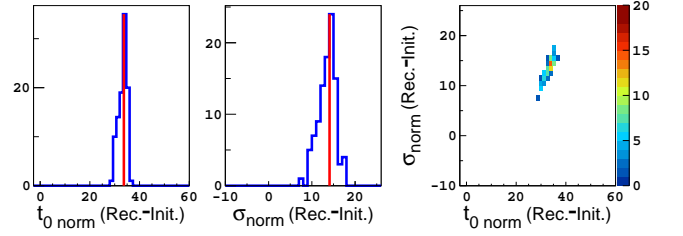


FIG. 44: Change in $t_{0\text{norm}}$ and σ_{norm} for protons from the fits in Fig. 41.

Data consisting of predominantly iron, such as the data sets fitted in this section, are easier to fit than data consisting of predominately protons and helium.

The ability of a $t_{0\text{norm}}$ and σ_{norm} fit of these parameterisations to reconstruct the general mass composition trend of data based on any of these three parameterisations, indicates that the normalisations of t_0 and σ are the most relevant differences between these parameterisations in regards to reconstructing the mass composition. The results of the $t_{0\text{norm}}$, σ_{norm} and mass fraction fits of the Auger FD X_{\max} data [9] are presented in Section VII.

B. Fitting $t_{0\text{norm}}$, B , σ_{norm} and the mass fractions

The coefficient B (which defines the energy dependence of t_0) can also be fitted with $t_{0\text{norm}}$ and σ_{norm} provided the data consists of an adequate dispersion of masses and statistics. This three-coefficient fit will generally be less precise than the two-coefficient fit of only $t_{0\text{norm}}$ and σ_{norm} . Fitting additional coefficients increases the degeneracy between the fitted variables, unless there is significant mass diversity and statistics. Our Epos-LHC,

QGSJetII-04 and Sibyll2.3 predictions of B are fairly similar among primaries, therefore we do not expect to see a significant improvement in the systematics of the reconstructed mass composition when adding B to our parameterisation fits of data based on any of these three models. However, it is possible that nature has a different energy dependence for t_0 (different from the three models), so by including B in the fit we reduce considerably the model dependence of the mass composition interpretation of the X_{\max} distributions.

Figs. 45 and 46 display the reconstructed mass composition and fitted coefficient values from fitting $t_{0\text{norm}}$, B and σ_{norm} of our Epos-LHC parameterisations to data generated from the Epos-LHC $t_{0\text{norm}}$ and σ_{norm} fit of the FD X_{\max} data set. Comparing this result to Fig. 27, the systematic offsets in the median reconstructed mass composition from the true mass for the three-coefficient fit are similar to the two-coefficient fit. Fig. 46 shows that the three fitted shape coefficients are accurately fitted and are well constrained.

However, as mentioned previously, data consisting of predominantly iron are easier to fit than data consisting of predominately proton and helium. The $t_{0\text{norm}}$, B , σ_{norm} and mass fraction fit of the latter data can result in a reconstructed mass composition which is considerably less accurate than a fit where B is fixed to the true value of the data. This is because the degeneracy between the fitted parameters can result in the fitted shape coefficients shifting away from the true values.

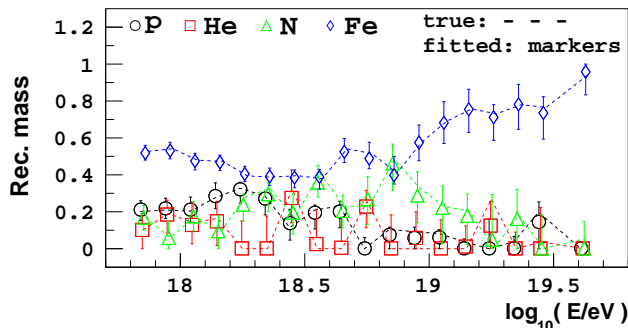


FIG. 45: Epos-LHC fit of X_{\max} data generated from the Epos-LHC parameterisation fit of Auger data.

C. Effect of X_{\max} systematic uncertainties when fitting $t_{0\text{norm}}$ and σ_{norm}

Fitting $t_{0\text{norm}}$ can compensate for systematic offsets in X_{\max} , while fitting σ_{norm} can compensate for systematic errors in the estimation of the detector resolution of X_{\max} . Figs. 47 and 48 shows the results of fitting the mass fractions, $t_{0\text{norm}}$ and σ_{norm} of our QGSJetII-04 parameterisation to 100 data sets generated from the parameterisation which resulted when the mass fractions, $t_{0\text{norm}}$ and σ_{norm} of the QGSJetII-04 parameterisation

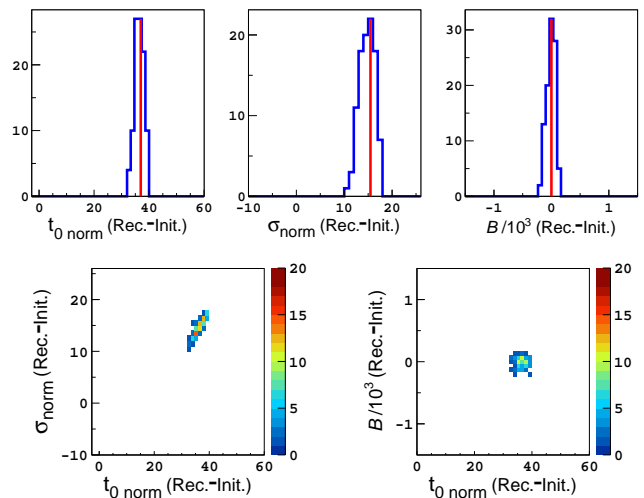


FIG. 46: Change in $t_{0\text{norm}}$, B and σ_{norm} for protons from the fits in Fig. 45.

were fitted to Auger FD X_{\max} data. Across the whole energy range, the mock data was shifted by a systematic offset of -10 g/cm^2 , and also smeared by a Gaussian distributed random variable of $\sigma = 10 \text{ g/cm}^2$ (this additional smearing is not accounted for in the resolution of the applied X_{\max} parameterisation), to test if the fit of $t_{0\text{norm}}$ and σ_{norm} can compensate for these systematics. The red lines in Fig. 48 indicate the true $t_{0\text{norm}}$ and σ_{norm} values of the data (relative to the initial QGSJetII-04 parameterisation being fitted) before the X_{\max} systematics were applied.

The mean shift in the fitted $t_{0\text{norm}}$ values from the original $t_{0\text{norm}}$ values of the data is $\sim -10 \text{ g/cm}^2$ (Fig. 48), to compensate mainly for the -10 g/cm^2 X_{\max} systematic offset applied to the data. As t_0 changes by the same amount for each primary when $t_{0\text{norm}}$ is fitted, and the X_{\max} systematic was applied consistently to all data, the $t_{0\text{norm}}$ fit is capable of completely accounting for the X_{\max} systematic offset. However, σ_{norm} for each primary is changed by different absolute amounts when fitting this coefficient, but all of the data is smeared (all masses are consistently smeared), consequently the correct σ_{norm} cannot be fitted for each primary, which may also effect the fit of $t_{0\text{norm}}$. The shift in σ_{norm} for protons from the original σ_{norm} is only $\sim +2 \text{ g/cm}^2$. Despite the fit of σ_{norm} being unable to thoroughly account for the 10 g/cm^2 systematic in the resolution, the absolute offsets in the median reconstructed mass fractions from the true mass are less than 10% in most energy bins, due to a combined shift of $t_{0\text{norm}}$ and σ_{norm} in the appropriate directions.

The accuracy of the reconstructed mass fractions from the fit of this shifted and smeared data is similar to the same fit of the un-shifted and un-smeared data in Fig. 34. Reasonable detector resolution systematics and systematic offsets in X_{\max} will not significantly effect the accu-

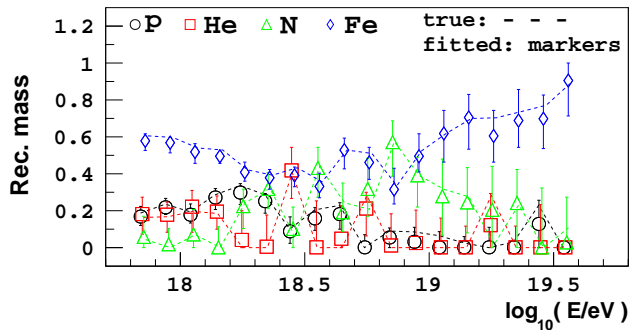


FIG. 47: Fits of $t_{0\text{norm}}$ and σ_{norm} to X_{max} data consisting of a -10 g/cm^2 systematic offset in X_{max} .

The X_{max} data was also smeared by a Gaussian distributed random variable of $\sigma = 10 \text{ g/cm}^2$, which was unaccounted for in the initial X_{max} parameterisation fitted.

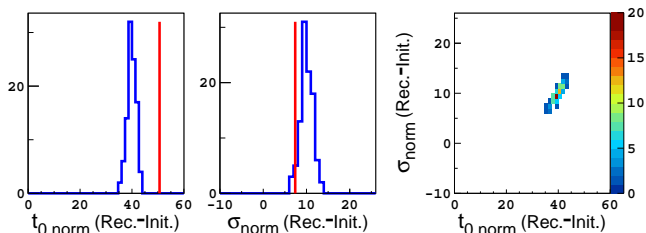


FIG. 48: Change in $t_{0\text{norm}}$ and σ_{norm} for protons from the fits in Fig. 47.

curacy of the reconstructed mass composition.

If the data was not smeared by a Gaussian random variable, and only shifted by a constant X_{max} offset, the $t_{0\text{norm}}$ and σ_{norm} fit of this shifted data would result in a change in the fitted $t_{0\text{norm}}$ (compared to the $t_{0\text{norm}}$ fitted to the un-shifted data) which is very close to the value of the X_{max} offset. Shifting the X_{max} data by a constant value has essentially the same effect on the fit as shifting the parameterisation by a constant value, with a very minuscule difference arising if the detector acceptance of X_{max} is not shifted by the same offset to account for the applied X_{max} offset (this is not an issue when fitting the measured Auger data).

VII. RESULTS

We have applied our Epos-LHC, QGSJetII-04 and Sibyll2.3 X_{max} parameterisations separately to X_{max} data measured by the Pierre Auger Observatory fluorescence detector (FD) [9].

Fig. 49 displays the results from fitting the mass fractions and the coefficients $t_{0\text{norm}}$ and σ_{norm} of our Epos-LHC, QGSJetII-04 and Sibyll2.3 X_{max} distribution parameterisations. The top three panels display the fitted mass fractions for each model, and the bottom panel

shows the p-values for these fits. The fits of these parameterisations to the X_{max} distributions are shown in Appendix B.

The p-value is defined as the probability of obtaining a worse fit (larger likelihood ratio \mathcal{L}) than that obtained with the data. The resulting parameterisation and fractions from the fit of the X_{max} distributions were used to generate sets of mock X_{max} distributions to determine the p-values, and to calculate the mass composition statistical errors. Fitting $t_{0\text{norm}}$ and σ_{norm} improves the goodness of the fit of the X_{max} distributions (bottom panel Fig. 49). This is evident by comparing the QGSJetII-04 p-values for the $t_{0\text{norm}}$ and σ_{norm} fit to the QGSJetII-04 p-values for the fit of only the mass fractions.

We find that the Epos-LHC, QGSJetII-04 and Sibyll2.3 parameterisation fits of the X_{max} distributions give a consistent mass composition result. Fig. 50 shows the corresponding moments of the $\ln A$ distribution. The results suggest a composition consisting of predominantly iron. Below $10^{18.8} \text{ eV}$, the small proportions of proton, helium and nitrogen vary. Above $10^{18.8} \text{ eV}$, there is little proton or helium, and with increasing energy the nitrogen component gradually gives way to the growing iron component, which dominates at the highest energies. There does not appear to be a distinct feature near the ankle ($\sim 10^{18.2} \text{ eV}$), where it is assumed cosmic rays transition from Galactic to extragalactic [14]. Considering the upper limits on the large scale anisotropy [15] indicate protons below $10^{18.5} \text{ eV}$ are most likely of extragalactic origin, the fitted proton fractions below the ankle are suitably small if cosmic rays below the ankle are Galactic. A significant modification of the hadronic models is required to accommodate a proton dominant composition above 10^{18} eV [16].

The first two moments of the Auger X_{max} distributions from [9] and their predictions (for proton and Fe) as a function of energy are shown in Fig. 51. It shows that the $t_{0\text{norm}}$ and σ_{norm} fits reduce the difference between the predictions from the Epos-LHC and QGSJetII-04 hadronic models. For t_0 and σ , the separation between the proton prediction and heavier nuclei is larger in the Sibyll2.3 parameterisation than the Epos-LHC or QGSJetII-04 parameterisations, consequently the Sibyll2.3 proton predictions from the fit are in disagreement with the two other parameterisations. The values of the coefficients in Equation (2) for proton, helium, nitrogen and iron primaries for the Epos-LHC, QGSJetII-04 and Sibyll2.3 models (assuming a normalisation energy of $E_0 = 10^{18.24} \text{ eV}$) can be found in Table I of Appendix C. The values fitted to the data for $t_{0\text{norm}}$ and σ_{norm} are also shown in Table I. The statistical errors in the estimated value of $\langle X_{\text{max}} \rangle$ for protons or iron over the energy range are the same as the statistical error in the fitted value of $t_{0\text{norm}}$, while for $\sigma(X_{\text{max}})$ the statistical error is less than 1 g/cm^2 for protons and iron.

The fitted values of $t_{0\text{norm}}$ are much larger than the initial parameterisation predictions, consequently the pre-

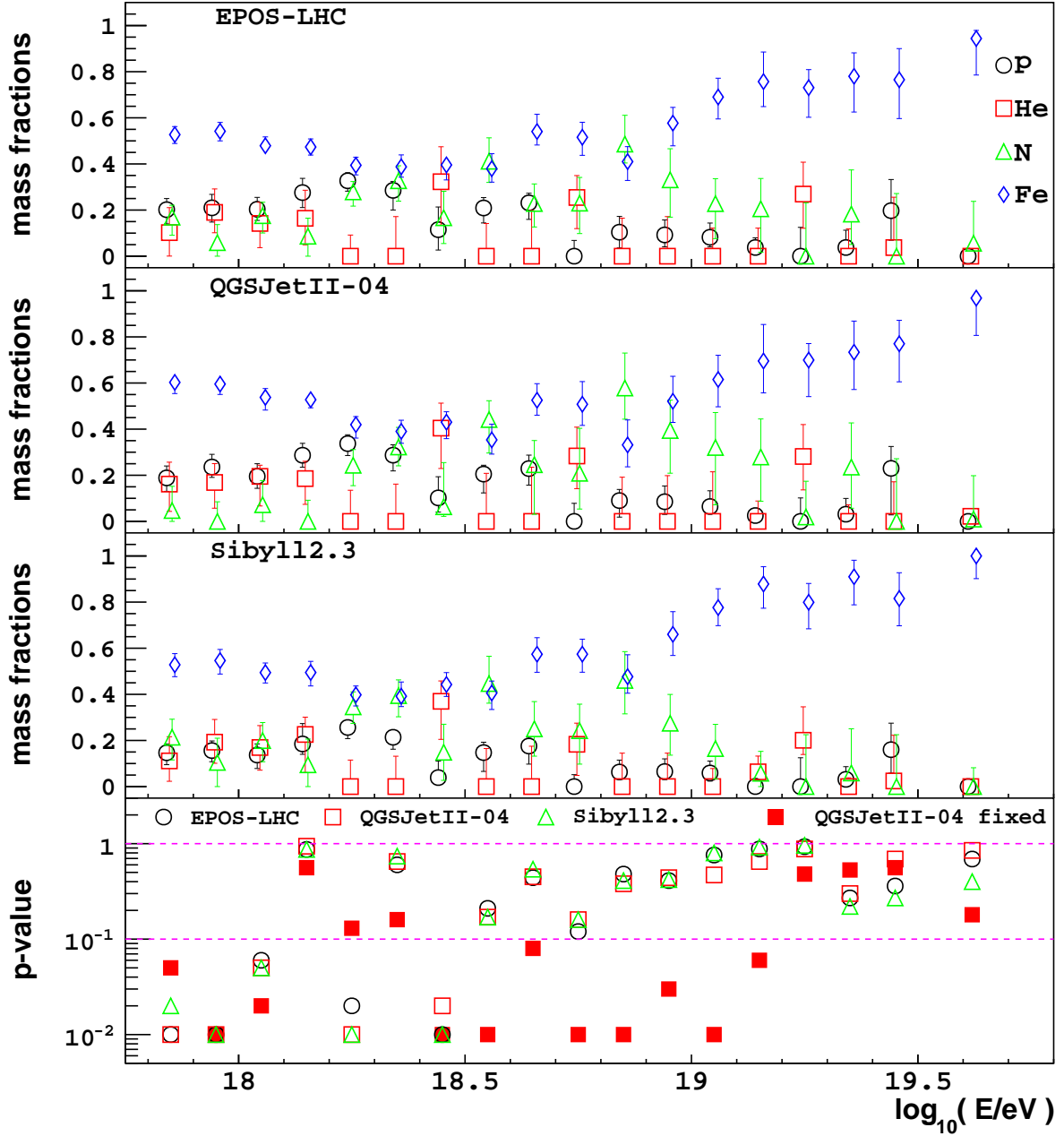


FIG. 49: Fitting $t_{0\text{norm}}$, σ_{norm} and the mass fractions of our parameterisations to FD X_{max} data measured by the Pierre Auger Observatory. The fitted mass fractions and p-values for each fitted model are shown. The red solid squares show the p-values for QGSJetII-04 when fitting only the mass fractions ($t_{0\text{norm}}$ and σ_{norm} fixed).

dicted $\langle X_{\text{max}} \rangle$ from the fits are much larger than the initial predictions. The fitted σ_{norm} values are also larger than the initial predictions, consequently the predicted $\sigma(X_{\text{max}})$ from the fit is larger. After the fit of $t_{0\text{norm}}$ and σ_{norm} , our Epos-LHC, QGSJetII-04 and Sibyll12.3 parameterisations still have different predictions for the X_{max} distribution shape properties as a function of mass and energy, but despite this there is reasonable agreement

on the reconstructed mass composition from these fits. An observed shift in the fitted values of $t_{0\text{norm}}$ and σ_{norm} from the initial parameterisation prediction could be due to the initial parameterisation inadequately describing nature, systematics in the measured X_{max} values, or a combination of both factors. Degeneracy between the fitted parameters could also contribute to a shift in the fitted coefficients, however the performance analysis in

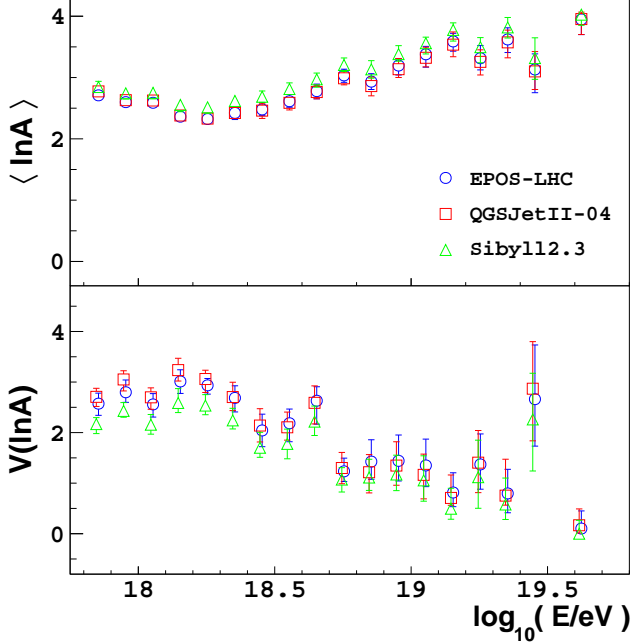


FIG. 50: First two moments of the $\ln A$ distribution estimated from the fitted fractions of the $t_{0\text{norm}}$, σ_{norm} and mass fraction fit of the FD X_{max} distributions measured by the Pierre Auger Observatory.

Section VI indicates that the results presented here are unlikely to be affected by degeneracy.

The mass composition results are sensitive to the assumed values of the X_{max} distribution properties which are not affected by the fit of $t_{0\text{norm}}$ and σ_{norm} (such as the elongation rate and the $\langle X_{\text{max}} \rangle$ separation between p and Fe). The results are also sensitive to the fitting range limits. As our knowledge of the hadronic physics occurring at the highest energies progresses, the coefficients which are fitted and the fitting range limits applied may change. For example, a reduced upper limit of $t_{0\text{norm}}$ would result in the $t_{0\text{norm}}$, σ_{norm} and mass fraction fit of the Auger data reconstructing a mass composition consisting of predominantly proton and helium. An increase in the statistics of the Auger X_{max} data, and/or an increased energy range, can reveal additional information regarding the shape coefficients.

Using the fitted values of $t_{0\text{norm}}$ and σ_{norm} , the parameters of the equations in [17], to convert the X_{max} moments into $\ln A$ moments, have been determined and are shown in Tables II and III of Appendix D.

Given the large $t_{0\text{norm}}$ and σ_{norm} values fitted to the Auger data when the mass fractions, $t_{0\text{norm}}$ and σ_{norm} are fitted, a second set of fits were performed where only $t_{0\text{norm}}$ and the mass fractions were fitted to the Auger data, using the same $t_{0\text{norm}}$ fitting range. These fits of the three parameterisations each used the standard QGSJetII-04 σ prediction. The resulting mass composi-

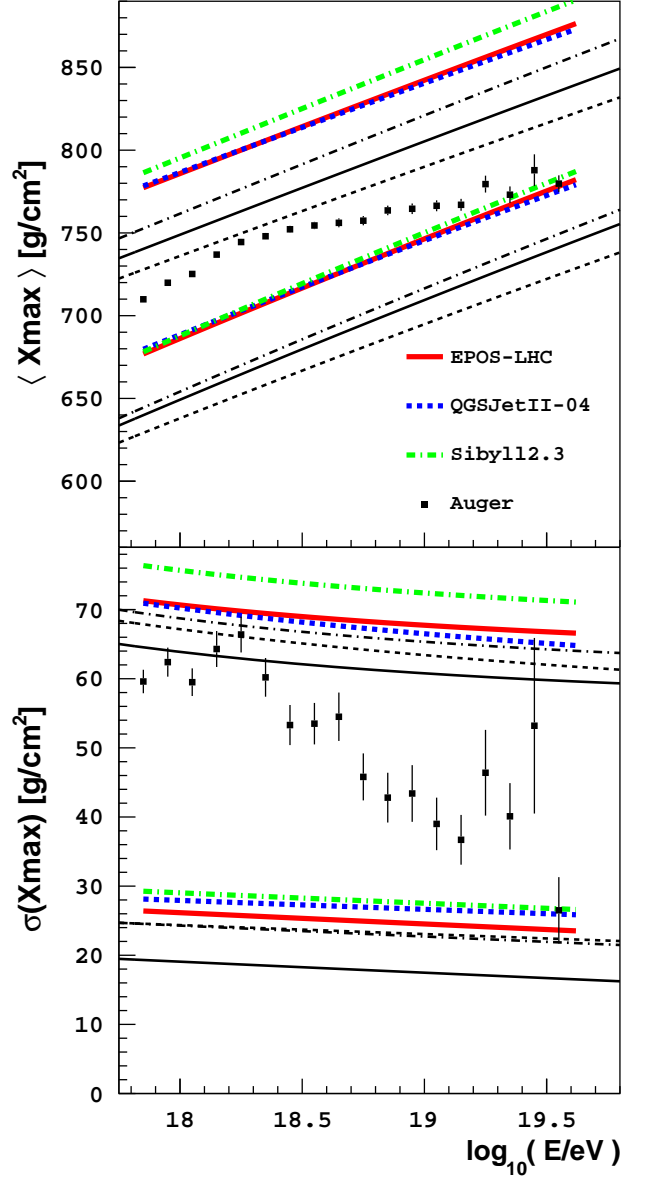


FIG. 51: The black lines show the $\langle X_{\text{max}} \rangle$ and $\sigma(X_{\text{max}})$ initially predicted by the X_{max} parameterisations for proton and iron. The red, blue and green lines show the new predictions for the $\langle X_{\text{max}} \rangle$ and $\sigma(X_{\text{max}})$ after fits of $t_{0\text{norm}}$, σ_{norm} and the mass fractions to FD X_{max} distributions measured by the Pierre Auger Observatory.

tion, $\ln A$ and X_{max} moments are shown in Figs. 52, 53 and 54 respectively. The fitted values of $t_{0\text{norm}}$ are shown in Table I of Appendix C, and using these values the parameters of the equations in [17] have been determined and are shown in Tables IV and V of Appendix D.

As the fitted values of $t_{0\text{norm}}$ are not as large compared

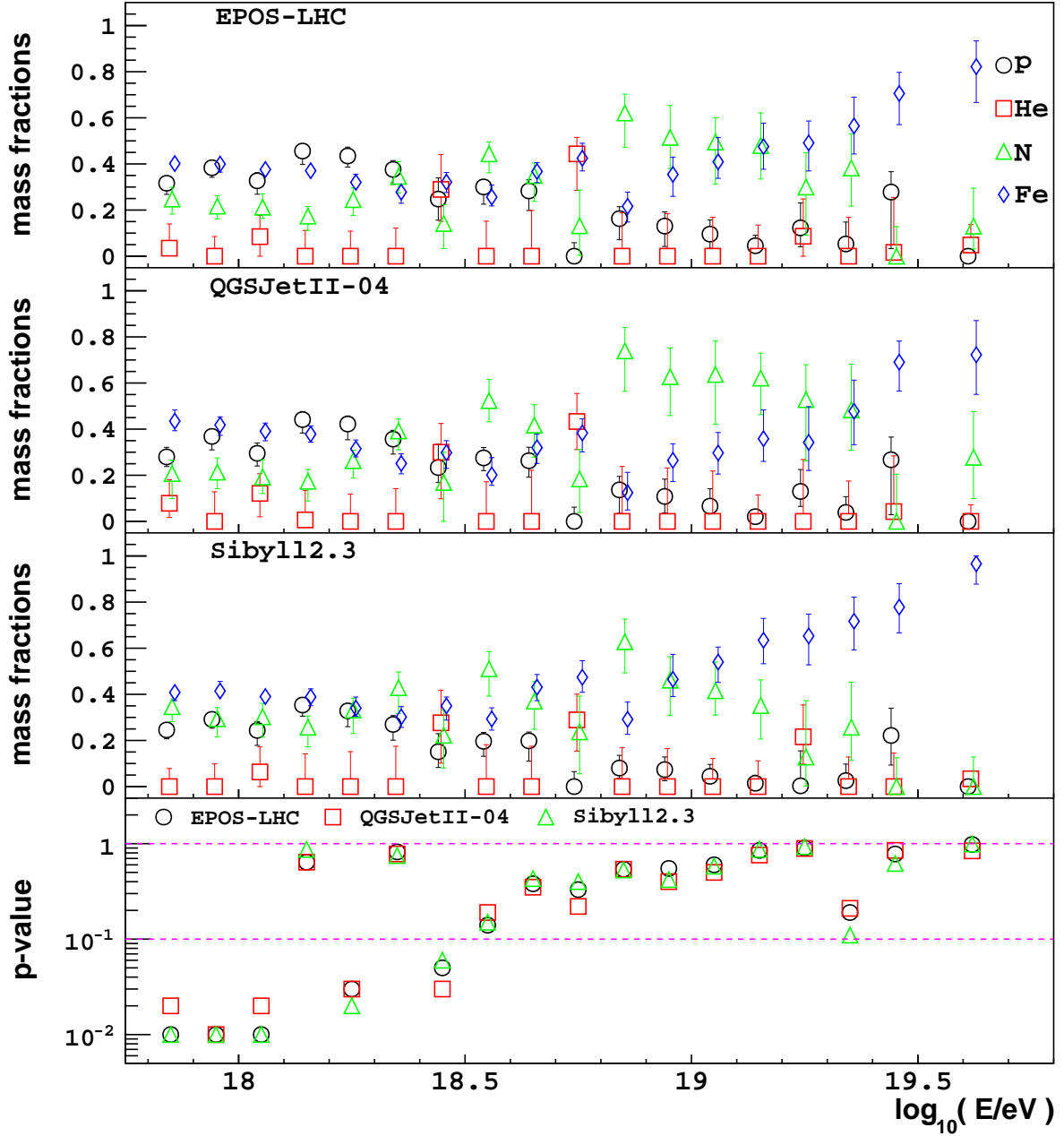


FIG. 52: Fitting $t_{0,\text{norm}}$ and the mass fractions of our parameterisations to FD X_{max} data measured by the Pierre Auger Observatory. The fitted mass fractions and p-values for each fitted model are shown.

to the two-coefficient fit, the predicted $\langle X_{\text{max}} \rangle$ of the fits are not as large, but still quite large compared to the initial parameterisation predictions. The reconstructed mass composition from the fits of only $t_{0,\text{norm}}$ (Fig. 52) consists of a larger abundance of nitrogen and protons, at the expense of iron and helium, compared to that of the $t_{0,\text{norm}}$ and σ_{norm} fit (Fig. 49). The general transition of the mass composition for the three parameterisations is consistent between the one-coefficient and two-coefficient fits.

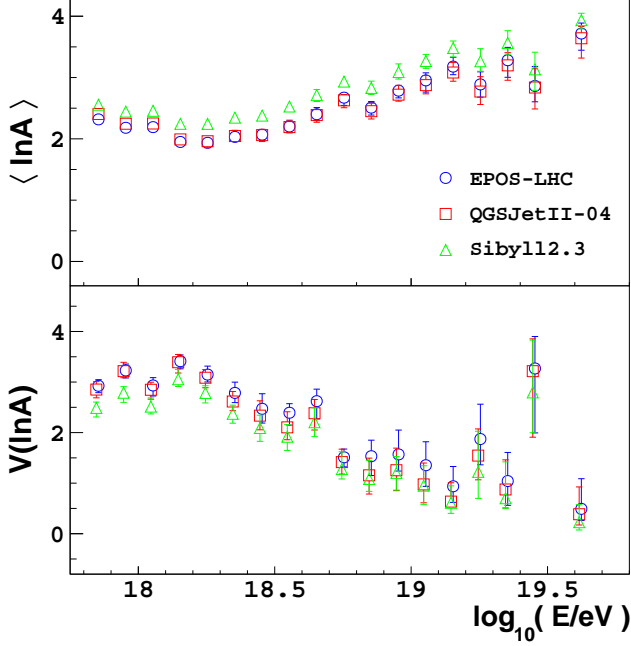


FIG. 53: First two moments of the $\ln A$ distribution estimated from the fitted fractions of the $t_{0\text{norm}}$ and mass fraction fit of the FD X_{max} distributions measured by the Pierre Auger Observatory.

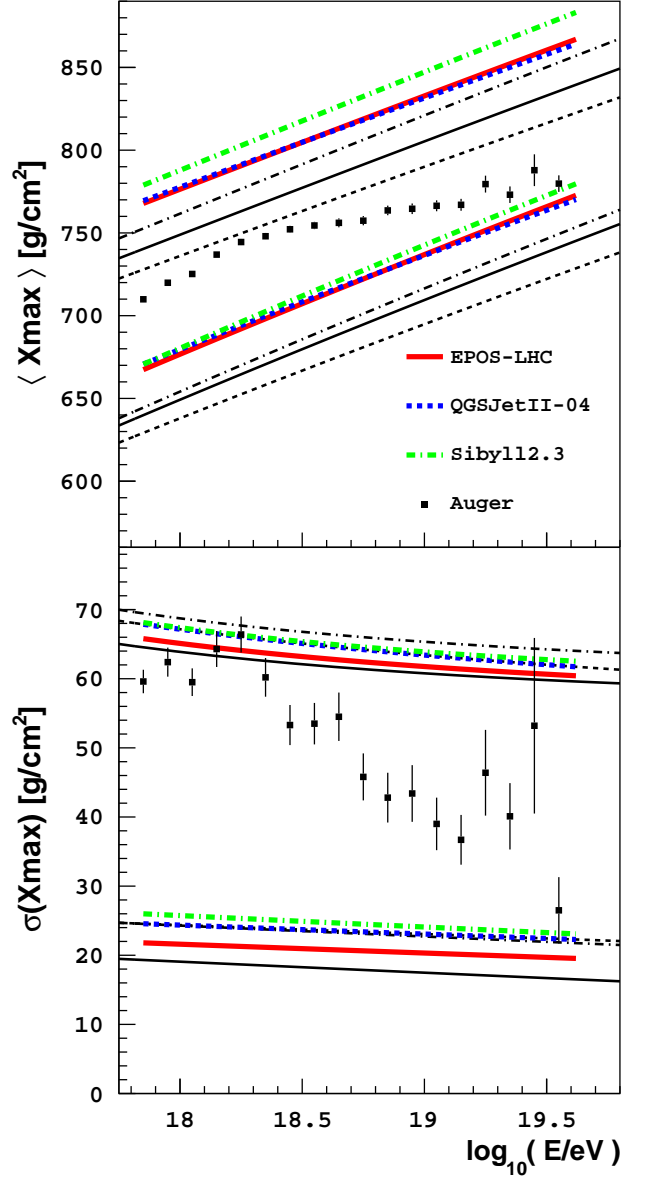


FIG. 54: The black lines show the $\langle X_{\text{max}} \rangle$ and $\sigma(X_{\text{max}})$ initially predicted by the X_{max} parameterisations for proton and iron. The red, blue and green lines show the new predictions for the $\langle X_{\text{max}} \rangle$ and $\sigma(X_{\text{max}})$ after fits of the mass fractions and $t_{0\text{norm}}$ (applying the standard QGSJetII-04 σ prediction) to FD X_{max} distributions measured by the Pierre Auger Observatory.

VIII. CONCLUSIONS

We have presented a novel method to estimate the mass composition (from X_{\max} distributions) which is less dependent on hadronic models. The method uses parameterisations of X_{\max} distributions according to different hadronic interaction models. Provided that the measured X_{\max} distributions consist of different primary masses and sufficient statistics over a large energy range (which seems to be the case for the Auger X_{\max} data), two shape coefficients, of the X_{\max} distribution parameterisation, can be fitted together with the mass fractions, reducing the model dependency in the mass composition interpretation (we have tested the Epos-LHC, QGSJetII-04 and Sibyll2.3 models). The main differences between the predicted X_{\max} distributions from different models are the normalisation values of the mode and spread for each primary. So, by fitting two coefficients ($t_{0,\text{norm}}$ and σ_{norm}) which adjust the normalisation of the mode and spread for each primary in an appropriate manner, the resulting mass composition is consistent for the three hadronic models tested here. A third coefficient, “ B ”,

which adjust the energy dependence of the $\langle X_{\max} \rangle$ can be fitted, further reducing the systematic model uncertainty in the fitted mass composition. However, given the current statistics and limited energy range of the published Auger X_{\max} distributions and the possible distribution of masses, fitting this third parameter may introduce large systematic uncertainties in the composition.

The mass fraction, $t_{0,\text{norm}}$ and σ_{norm} fits reconstruct a mass composition trend with energy that is consistent between the three models. There is a dominant abundance of iron over the energy range, particularly at the highest energies where there is almost pure iron. By fitting only $t_{0,\text{norm}}$ and adopting the QGSJetII-04 σ prediction for the three models, the relative abundance of protons increases.

The results are sensitive to the other model parameters that we keep fixed, such as the elongation rate and the $\langle X_{\max} \rangle$ separation between p and Fe. It is important to note that systematics in the measured X_{\max} values are absorbed by the fits of $t_{0,\text{norm}}$ and σ_{norm} . Thus, the composition fractions are not significantly affected by systematics in X_{\max} .

-
- [1] T. K. Gaisser and A. M. Hillas, Proc. 15th ICRC **8**, 353 (1977).
 - [2] K.-H. Kampert and M. Unger, Astropart. Phys. **35**, 660 (2012), arXiv:1201.0018 [astro-ph.HE].
 - [3] P. Abreu *et al.* (Pierre Auger), Phys. Rev. Lett. **109**, 062002 (2012), arXiv:1208.1520 [hep-ex].
 - [4] T. Bergmann, R. Engel, D. Heck, N. N. Kalmykov, S. Ostapchenko, T. Pierog, T. Thouw, and K. Werner, Astropart. Phys. **26**, 420 (2007), arXiv:astro-ph/0606564 [astro-ph].
 - [5] T. Pierog *et al.*, Nucl. Phys. Proc. Suppl. **151**, 159 (2006), astro-ph/0411260.
 - [6] T. Pierog, I. Karpenko, J. M. Katzy, E. Yatsenko, and K. Werner, Phys. Rev. **C92**, 034906 (2015), arXiv:1306.0121 [hep-ph].
 - [7] S. Ostapchenko, Phys. Rev. **D83**, 014018 (2011), arXiv:1010.1869 [hep-ph].
 - [8] F. Riehn, R. Engel, A. Fedynitch, T. K. Gaisser, and T. Stanev, PoS(ICRC2015) **558** (2016).
 - [9] A. Aab *et al.* (Pierre Auger), Phys. Rev. **D90**, 122005 (2014), arXiv:1409.4809 [astro-ph.HE].
 - [10] A. Aab *et al.* (Pierre Auger), Phys. Rev. **D90**, 122006 (2014), arXiv:1409.5083 [astro-ph.HE].
 - [11] A. Aab *et al.* (Pierre Auger), JCAP **1704**, 038 (2017), arXiv:1612.07155 [astro-ph.HE].
 - [12] C. J. Todero Peixoto, V. de Souza, and J. A. Bellido, Astropart. Phys. **47**, 18 (2013), arXiv:1301.5555 [astro-ph.HE].
 - [13] B. Peters, Nuovo Cimento **22**, 800 (1961).
 - [14] J. Linsley, Proc. 8th ICRC **4**, 77 (1963).
 - [15] Pierre Auger Collaboration, Astrophys. J Suppl. **203**, 34 (2012), arXiv:1210.3736 [astro-ph.HE].
 - [16] V. S. Berezinsky and S. I. Grigor’eva, Astron. Astrophys. **199**, 1 (1988).
 - [17] P. Abreu *et al.* (Pierre Auger), JCAP **1302**, 026 (2013), arXiv:1301.6637 [astro-ph.HE].

Appendix A: Fits to X_{\max} distributions

The fits of Equation (1) to energy binned X_{\max} data are shown in Figs. 55, 56 and 57. The differences in the $\langle X_{\max} \rangle$ and $\sigma(X_{\max})$ of the data versus the fitted equation are shown in Fig. 58. For the fitted equation, $\langle X_{\max} \rangle_{\text{fit}} = t_0 + \lambda$ and $\sigma(X_{\max})_{\text{fit}} = \sqrt{\sigma^2 + \lambda^2}$. Although the fitted function (red line) does not always precisely overlap the data (blue line), we see $\langle X_{\max} \rangle_{\text{fit}}$ is always within 0.1 g/cm² of $\langle X_{\max} \rangle_{\text{data}}$. The $\langle X_{\max} \rangle$ of the distribution is the main property we endeavour to accurately define. $\sigma(X_{\max})_{\text{fit}}$ is always within 3 g/cm² of $\sigma(X_{\max})_{\text{data}}$ which is acceptable.

1. Epos-LHC X_{\max} distribution fits

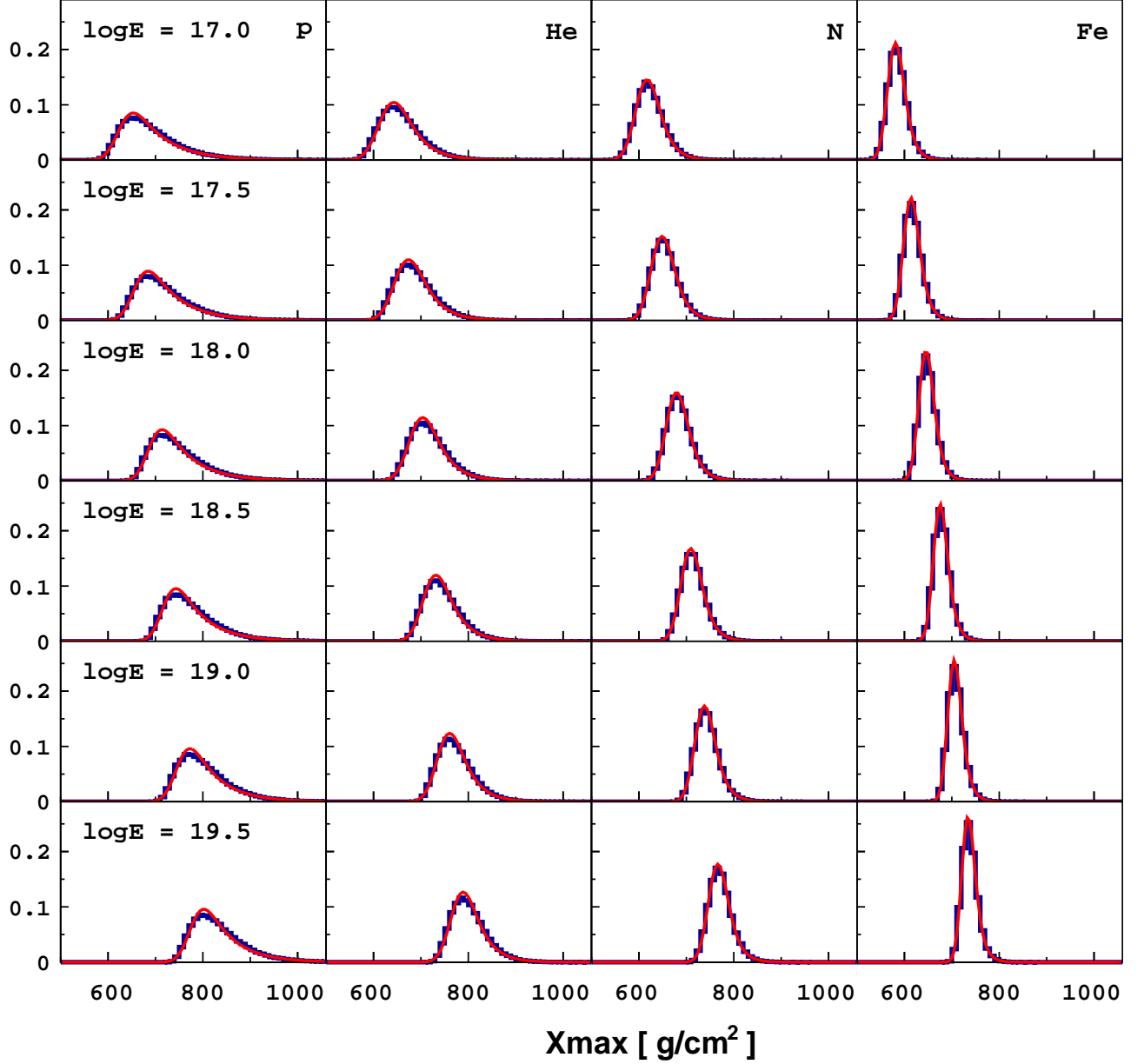


FIG. 55: Energy binned Epos-LHC X_{\max} distributions (blue line) fitted with Equation (1) (red line).

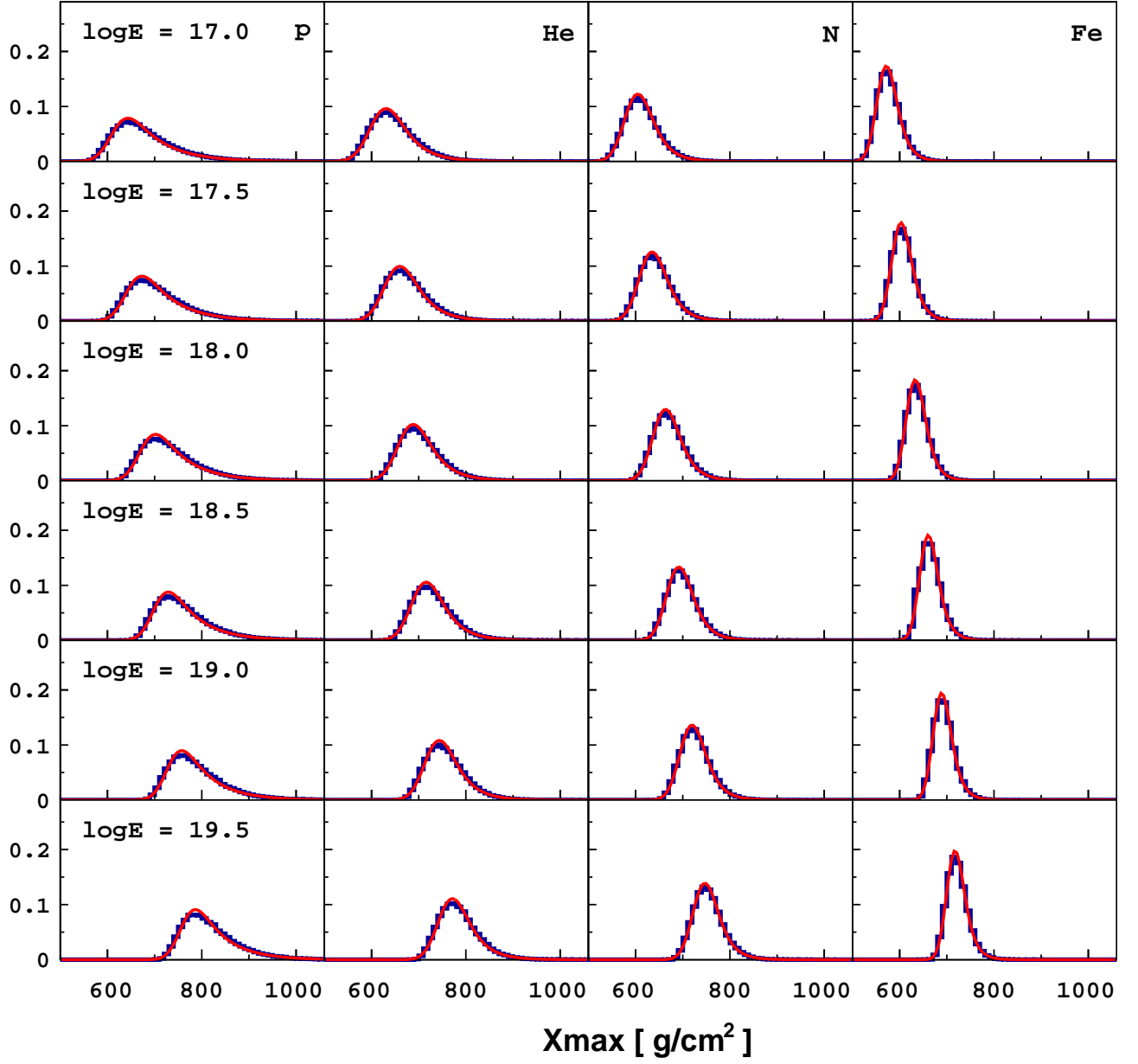
2. QGSJetII-04 X_{\max} distribution fits

FIG. 56: Energy binned QGSJetII-04 X_{\max} distributions (blue line) fitted with Equation (1) (red line).

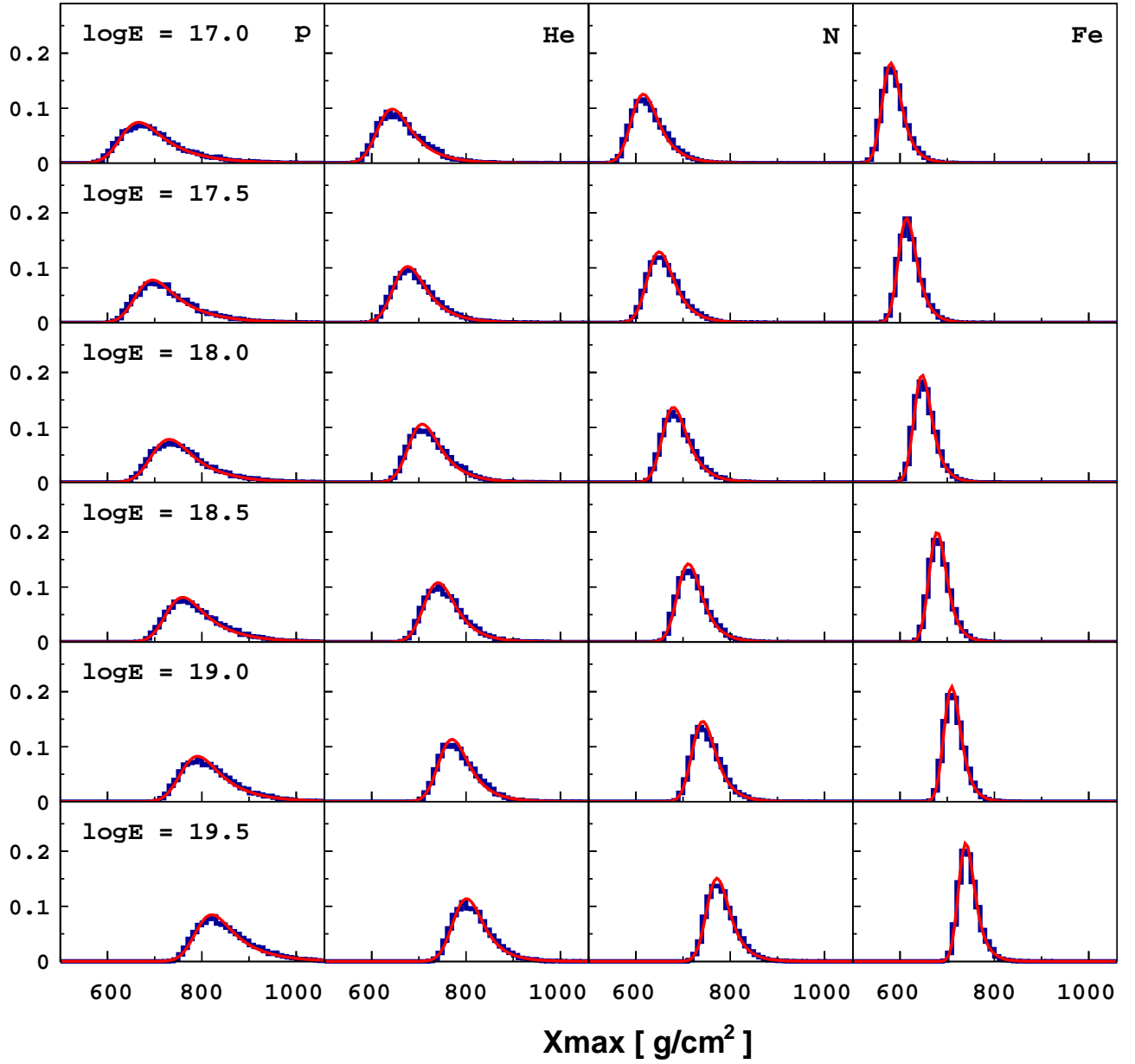
3. Sibyll2.3 X_{\max} distribution fits

FIG. 57: Energy binned Sibyll2.3 X_{\max} distributions (blue line) fitted with Equation (1) (red line).

4. X_{\max} moment comparison between the fitted parameterisation and the data

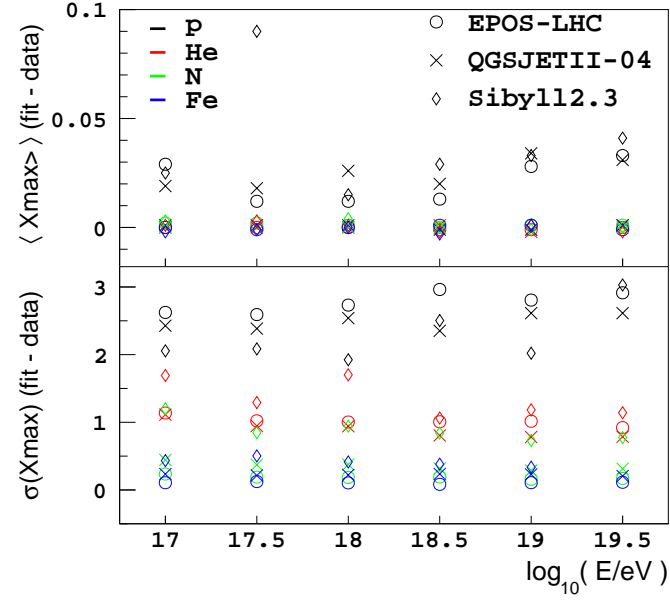


FIG. 58: Difference in the $\langle X_{\max} \rangle$ and $\sigma(X_{\max})$ between the data and the fitted equation.

Appendix B: Mass fraction, $t_{0\text{norm}}$ and σ_{norm} fits of the Auger FD X_{max} data

The $t_{0\text{norm}}$, σ_{norm} and mass fraction fits of each parameterisation to the Auger FD X_{max} distributions are shown in the following plots. The magenta lines illustrate the measured X_{max} distributions, while the teal lines illustrate the fitted parameterisation. The black, red, green and blue lines are the fitted proton, helium, nitrogen and iron parameterisations respectively.

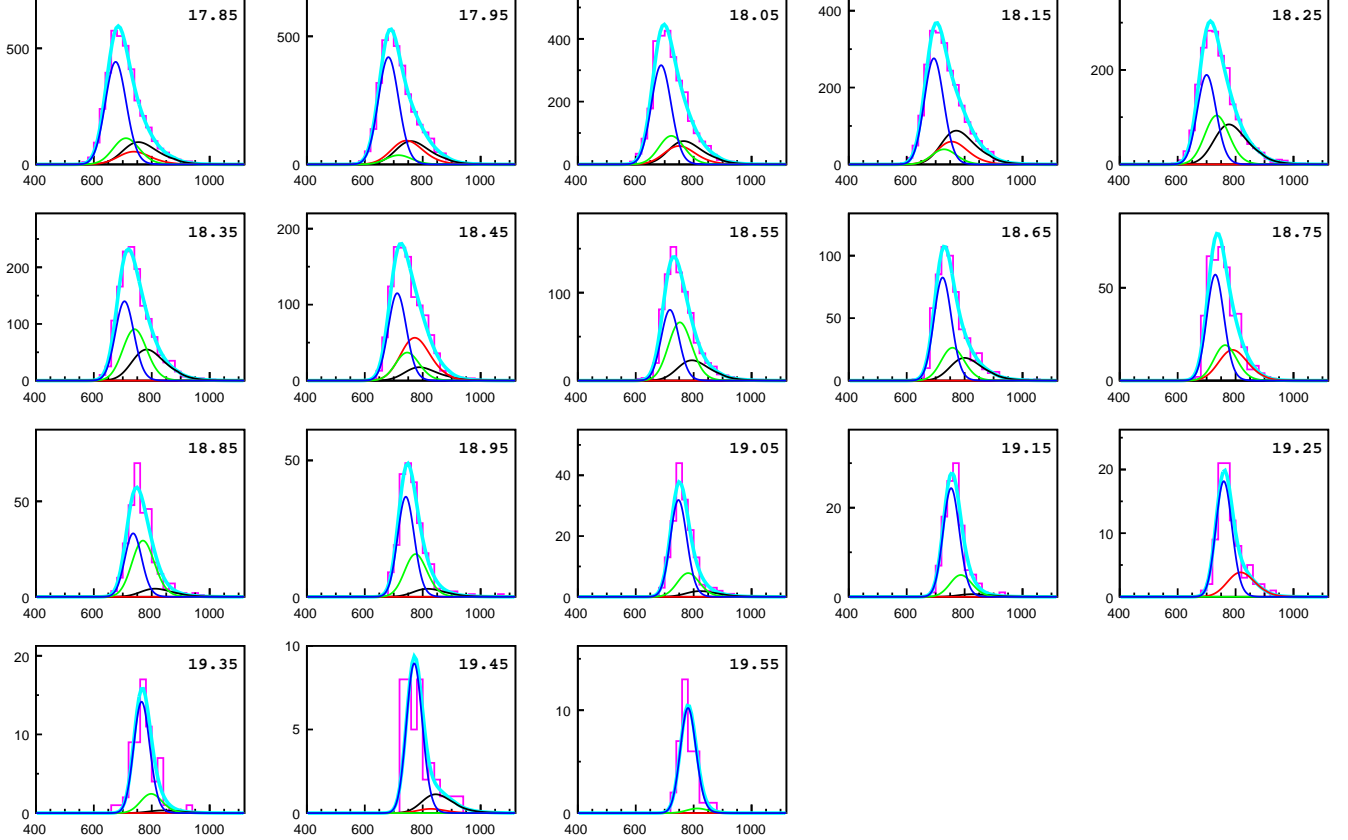


FIG. 59: Fit of the Epos-LHC X_{max} parameterisation.

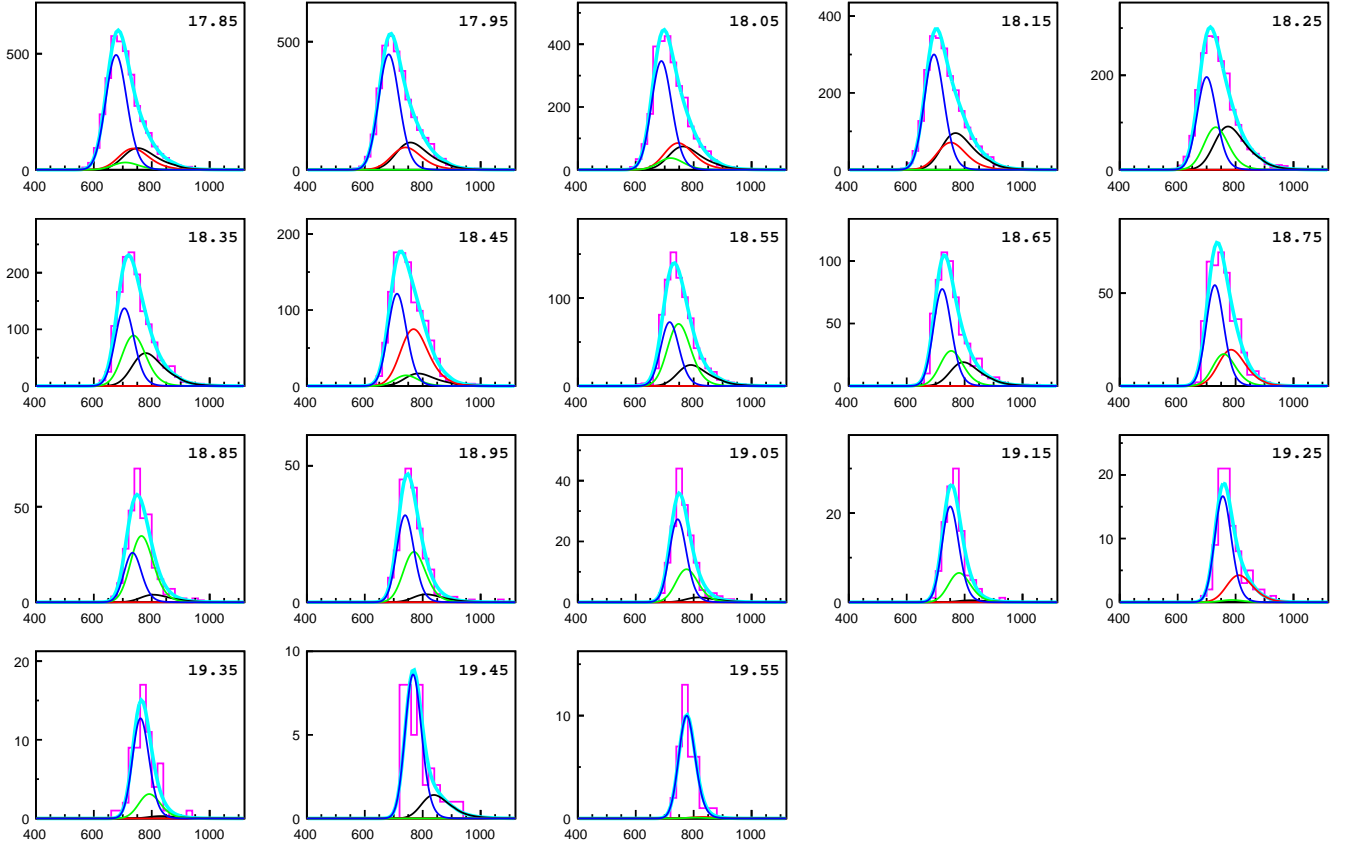


FIG. 60: Fit of the QGSJetII-04 X_{\max} parameterisation.

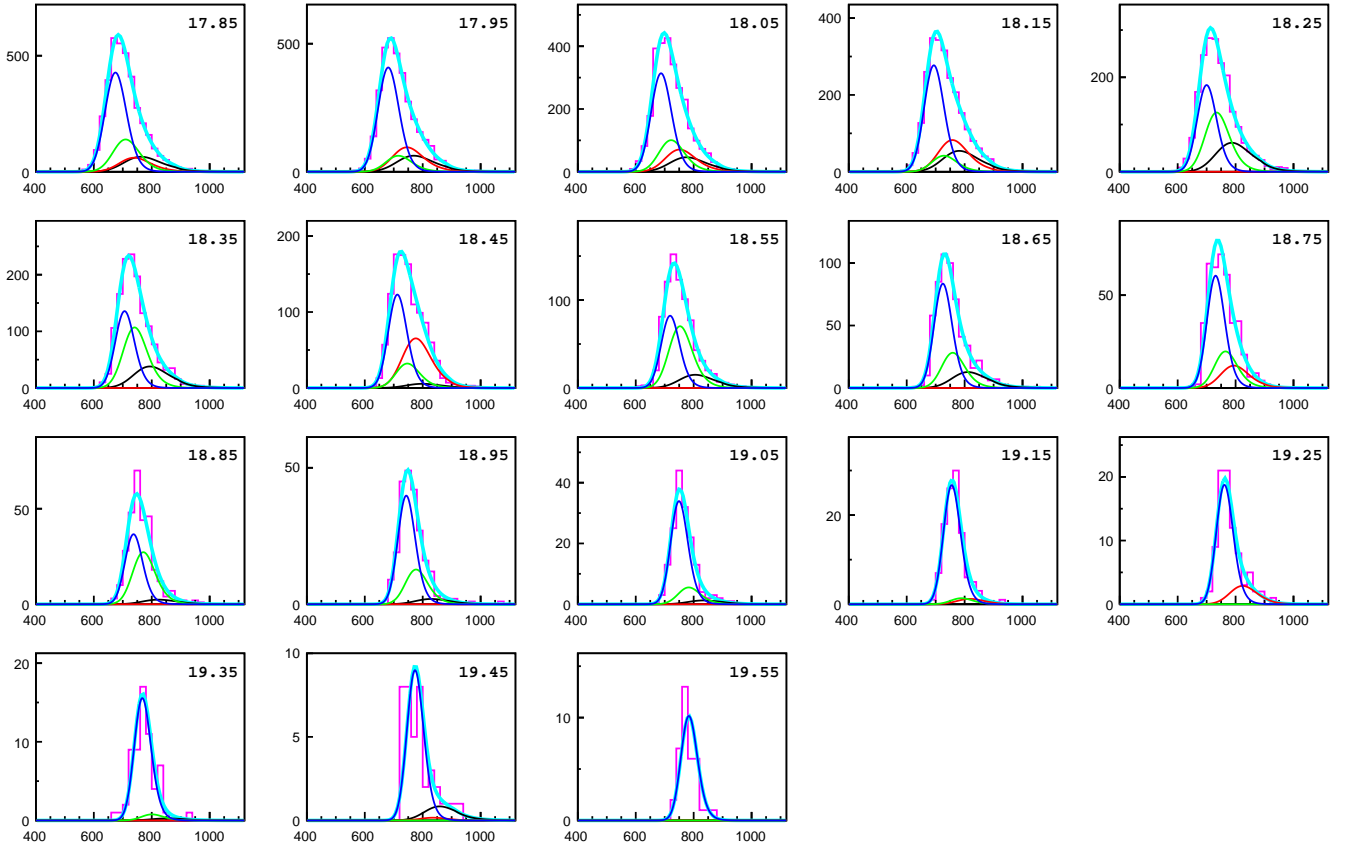


FIG. 61: Fit of the Sibyll2.3 X_{\max} parameterisation.

Appendix C: Table of coefficients for the X_{\max} distribution parameterisations

TABLE I: Coefficients of Equation (2) for the Epos-LHC, QGSJetII-04 and Sibyll2.3 X_{\max} distribution predictions, assuming a normalisation energy of $E_0 = 10^{18.24}$ eV. Also in the table, we show the $t_{0\text{norm}}$ and σ_{norm} fitted to the Auger data from the $t_{0\text{norm}}$, σ_{norm} and mass fraction fit of each of the three models, and the $t_{0\text{norm}}$ fitted to the Auger data from the $t_{0\text{norm}}$ and mass fraction fit of each model.

Epos-LHC	Proton	Helium	Nitrogen	Iron
$t_{0\text{norm}}$	703	697	680	650
B	2533.29	2515.46	2548.31	2603.31
σ_{norm}	21.61	23.46	19.01	13.01
C	-0.63	-1.81	-1.67	-1.36
λ_{norm}	59.12	34.74	20.06	13.41
K	5.80	-1913.99	-1828.11	-1406.72
L	-25.93	0.063	0.035	0.027
fitted $t_{0\text{norm}}$	740 (stat.) $^{+2}_{-2}$	734	717	688
fitted σ_{norm}	37 (stat.) $^{+2}_{-1}$	40	32	22
fitted $t_{0\text{norm}}$ only	731 (stat.) $^{+1}_{-1}$	725	708	678
QGSJetII-04	Proton	Helium	Nitrogen	Iron
$t_{0\text{norm}}$	688	679	660	635
B	2444.88	2410.38	2422.37	2460.32
σ_{norm}	24.82	26.83	23.07	16.54
C	-1.32	-1.24	-0.99	-0.91
λ_{norm}	61.29	37.5	25.84	17.46
K	9.35	19.32	-1818.36	-986.08
L	-17.63	-6.08	0.041	0.040
fitted $t_{0\text{norm}}$	738 (stat.) $^{+1}_{-1}$	730	711	685
fitted σ_{norm}	32 (stat.) $^{+1}_{-1}$	35	30	21
fitted $t_{0\text{norm}}$ only	729 (stat.) $^{+1}_{-1}$	721	702	676
Sibyll2.3	Proton	Helium	Nitrogen	Iron
$t_{0\text{norm}}$	715	701	678	650
B	2666.31	2705.43	2695.22	2714.41
σ_{norm}	28.30	24.28	19.61	14.24
C	-1.08	-0.82	-1.20	-0.77
λ_{norm}	61.52	40.31	29.48	19.20
K	5.81	23.70	-1362.17	-1349.93
L	-27.47	-6.84	0.083	0.044
fitted $t_{0\text{norm}}$	748 (stat.) $^{+1}_{-2}$	735	712	684
fitted σ_{norm}	42 (stat.) $^{+1}_{-2}$	36	29	21
fitted $t_{0\text{norm}}$ only	741 (stat.) $^{+1}_{-1}$	727	704	676

Appendix D: X_{\max} moments in terms of $\ln A$ moments.

The first two X_{\max} moments can be parameterised in terms of $\ln A$ as follows [17]:

$$\langle X_{\max} \rangle = X_0 + D \log 10 \left(\frac{E}{E_0 A} \right) + \xi \ln A + \delta \ln A \log 10 \left(\frac{E}{E_0} \right), \quad (\text{D1})$$

and

$$\sigma^2(X_{\max}) = \sigma_p^2 [1 + a \langle \ln A \rangle + b \langle (\ln A)^2 \rangle], \quad (\text{D2})$$

where

$$\begin{aligned} \sigma_p^2 &= p_0 + p_1 \log 10 \left(\frac{E}{E_0} \right) + p_2 \left[\log 10 \left(\frac{E}{E_0} \right) \right]^2, \\ a &= a_0 + a_1 \log 10 \left(\frac{E}{E_0} \right). \end{aligned} \quad (\text{D3})$$

Using the $t_{0\text{norm}}$ and σ_{norm} fit results of the 2014 FD dataset (see Table I), the parameters of Equations (D1), (D2) and (D3) have been determined, and are displayed in Tables II and III. The mean and maximum $\langle X_{\max} \rangle$ residuals of the fit are $\sim 1 \text{ g/cm}^2$ and $\sim 2.5 \text{ g/cm}^2$ respectively. The mean and maximum $\sigma(X_{\max})$ residuals of the fit are $\sim 1 \text{ g/cm}^2$ and $\sim 1.5 \text{ g/cm}^2$ respectively.

parameter	Epos-LHC	QGSJetII-04	Sibyll2.3
X_0	842.8 ± 0.3	839.9 ± 0.3	855.7 ± 0.4
D	54.8 ± 0.5	51.9 ± 0.4	59.1 ± 0.6
ξ	-0.10 ± 0.26	-1.52 ± 0.20	0.09 ± 0.33
δ	0.83 ± 0.21	0.13 ± 0.16	1.20 ± 0.26

TABLE II: Parameters of Equation (D1), obtained by fitting the predicted $\langle X_{\max} \rangle$ from the $t_{0\text{norm}}$ and σ_{norm} fit of the 2014 FD data set. All values are in g/cm^2 .

parameter	Epos-LHC	QGSJetII-04	Sibyll2.3
$p_0 \times \text{g}^{-2} \text{cm}^4$	4592 ± 19	4402 ± 32	5222 ± 34
$p_1 \times \text{g}^{-2} \text{cm}^4$	-361 ± 20	-427 ± 33	-413 ± 35
$p_2 \times \text{g}^{-2} \text{cm}^4$	70 ± 33	71 ± 54	87 ± 56
a_0	-0.377 ± 0.003	-0.372 ± 0.005	-0.362 ± 0.004
a_1	-0.0038 ± 0.0010	-0.0004 ± 0.0017	-0.0031 ± 0.0016
b	0.040 ± 0.001	0.041 ± 0.001	0.038 ± 0.001

TABLE III: Parameters of Equation (D2) and Equation (D3), obtained by fitting the predicted $\sigma^2(X_{\max})$ from the $t_{0\text{norm}}$ and σ_{norm} fit of the 2014 FD data set.

Using the results from the fit of only $t_{0\text{norm}}$ and the mass fractions to the 2014 FD dataset (see Table I), the parameters of Equations (D1), (D2) and (D3) are displayed in Tables IV and V. The $\langle X_{\text{max}} \rangle$ and $\sigma(X_{\text{max}})$ residuals of these results are similar to those from the $t_{0\text{norm}}$, σ_{norm} and mass fraction fit results.

parameter	Epos-LHC	QGSJetII-04	Sibyll2.3
X_0	833.4 ± 0.3	830.9 ± 0.3	848.2 ± 0.4
D	54.8 ± 0.5	51.9 ± 0.4	59.1 ± 0.6
ξ	-0.10 ± 0.26	-1.52 ± 0.20	0.09 ± 0.33
δ	0.83 ± 0.21	0.13 ± 0.16	1.20 ± 0.26

TABLE IV: Parameters of Equation (D1), obtained by fitting the predicted $\langle X_{\text{max}} \rangle$ from the $t_{0\text{norm}}$ fit of the 2014 FD data set

parameter	Epos-LHC	QGSJetII-04	Sibyll2.3
$p_0 \times \text{g}^{-2}\text{cm}^4$	3793 ± 35	3990 ± 44	4049 ± 47
$p_1 \times \text{g}^{-2}\text{cm}^4$	-355 ± 36	-411 ± 45	-392 ± 49
$p_2 \times \text{g}^{-2}\text{cm}^4$	76 ± 61	74 ± 76	89 ± 80
a_0	-0.459 ± 0.006	-0.425 ± 0.007	-0.392 ± 0.008
a_1	-0.0022 ± 0.0021	-0.0011 ± 0.0026	-0.0041 ± 0.0027
b	0.059 ± 0.002	0.052 ± 0.002	0.045 ± 0.002

TABLE V: Parameters of Equation (D2) and Equation (D3), obtained by fitting the predicted $\sigma^2(X_{\text{max}})$ from the $t_{0\text{norm}}$ fit of the 2014 FD data set